AGU PUBLICATIONS

Journal of Geophysical Research: Space Physics

RESEARCH ARTICLE
10.1002/2015JA021728

Key Points:
- Magnetosphere-ionosphere coupling is key in diffuse auroral electron distribution function formation
- We present the solution of the Boltzman-Landau kinetic equation
- It is important to consider the coupled ionosphere-magnetosphere system

Correspondence to:
G. V. Khazanov,
george.v.khazanov@nasa.gov

Citation:
Khazanov, G. V., A. K. Tripathi, D. Sibeck, E. Himwich, A. Glocer, and R. P. Singhal (2015), Electron distribution function formation in regions of diffuse aurora, *J. Geophys. Res. Space Physics*, *120*, 9891–9915, doi:10.1002/2015JA021728.

Received 27 JUL 2015
Accepted 16 OCT 2015
Accepted article online 19 OCT 2015
Published online 13 NOV 2015

Electron distribution function formation in regions of diffuse aurora

G. V. Khazanov[1], A. K. Tripathi[2], D. Sibeck[1], E. Himwich[3], A. Glocer[1], and R. P. Singhal[2]

[1]NASA Goddard Space Flight Center, Greenbelt, Maryland, USA, [2]Department of Physics, Indian Institute of Technology (Banaras Hindu University), Varanasi, India, [3]Department of Physics, Yale University, New Haven, Connecticut, USA

Abstract The precipitation of high-energy magnetospheric electrons ($E \sim 600$ eV–10 KeV) in the diffuse aurora contributes significant energy flux into the Earth's ionosphere. To fully understand the formation of this flux at the upper ionospheric boundary, ~700–800 km, it is important to consider the coupled ionosphere-magnetosphere system. In the diffuse aurora, precipitating electrons initially injected from the plasma sheet via wave-particle interaction processes degrade in the atmosphere toward lower energies and produce secondary electrons via impact ionization of the neutral atmosphere. These precipitating electrons can be additionally reflected upward from the two conjugate ionospheres, leading to a series of multiple reflections through the magnetosphere. These reflections greatly influence the initially precipitating flux at the upper ionospheric boundary (700–800 km) and the resultant population of secondary electrons and electrons cascading toward lower energies. In this paper, we present the solution of the Boltzman-Landau kinetic equation that uniformly describes the entire electron distribution function in the diffuse aurora, including the affiliated production of secondary electrons ($E < 600$ eV) and its energy interplay in the magnetosphere and two conjugated ionospheres. This solution takes into account, for the first time, the formation of the electron distribution function in the diffuse auroral region, beginning with the primary injection of plasma sheet electrons via both electrostatic electron cyclotron harmonic waves and whistler mode chorus waves to the loss cone, and including their subsequent multiple atmospheric reflections in the two magnetically conjugated ionospheres. It is demonstrated that magnetosphere-ionosphere coupling is key in forming the electron distribution function in the diffuse auroral region.

1. Introduction

The diffuse aurora accounts for about 75% of the auroral energy that precipitates into the ionosphere [e.g., *Sandford*, 1968; *Newell et al.*, 2009], and its origin has recently been the subject of many discussions and publications. It is accepted that the diffuse aurora is the result of pitch angle scattering of plasma sheet electrons into the loss cone by different kinds of wave-particle interaction (WPI) processes [e.g., *Belmont et al.*, 1984; *Lyons*, 1984; *Roeder and Koons*, 1989; *Johnstone et al.*, 1993]. Electron cyclotron harmonic (ECH) waves and whistler mode chorus waves resonate with electrons in the energy range from 100 eV to several keV and have been associated with enhanced flux of low-energy electrons [*Lui et al.*, 1977; *Anderson and Maeda*, 1977; *Ni et al.*, 2008; *Meredith et al.*, 2009].

Ions and electrons both precipitate during the diffuse aurora; however, the average integral number flux of precipitating auroral ions is usually 1 to 2 orders of magnitude less than the average integral number flux of precipitating auroral electrons [*Hardy et al.*, 1985, 1989], which is why this paper focuses only on electron precipitation.

ECH waves are electrostatic emissions observed in bands between the different harmonics of electron gyrofrequency, f_{ce}, and are sometimes called "$n + \frac{1}{2}$" waves because the emissions typically appear close to the odd integral half harmonics of the f_{ce} [e.g., *Kennel et al.*, 1970]. ECH waves are generally excited near the magnetic equator outside of the plasmapause and propagate at angles that are very large with respect to the ambient magnetic field. Whistler mode chorus waves are electromagnetic emissions with frequency below f_{ce}. Chorus waves range in frequency from 0.1 to 0.8 f_{ce} and typically occur within two distinct frequency bands, a lower and an upper band, with a gap in wave power at 0.5 f_{ce} [e.g., *Burtis and Helliwell*, 1969]. Chorus waves predominantly propagate parallel or quasi-parallel to the ambient magnetic field. Their intensity depends strongly on geomagnetic activity. Previous work [*Su et al.*, 2009, 2010; *Thorne et al.*, 2010] has shown that resonant scattering by upper band chorus (UBC) is capable of causing ~100 eV to ~2 keV electrons to precipitate into the loss cone. By contrast, lower band chorus (LBC) waves are most effective in causing precipitation of >2 keV plasma sheet electrons. *Su et al.* [2010] also find that whistler mode chorus waves are more effective at producing diffuse aurora at larger L shells. This is generally consistent with previous statistical results [*Meredith et al.*, 1999] and suggests that whistler mode waves are a dominant cause of pancake distribution formation outside $L = 6.0$, whereas inside $L = 6.0$, and particularly, near the plasmapause, ECH waves also make a significant contribution.

As a consequence, both ECH and whistler waves should be considered in any explanation of the diffuse aurora. More recent studies by *Ni et al.* [2012] and *Zhang et al.* [2015] support the scenario that ECH emissions can be a large or even dominant driving source of diffuse auroral precipitation in the outer magnetosphere ($L > 8$), while whistler mode chorus waves are mainly responsible for the occurrences of the diffuse aurora in the inner magnetosphere ($L < 8$). This owes to the fact that only chorus can explain the observations of a pancake electron distribution, which occur after electrons at small pitch angles are scattered into the loss cone [*Thorne et al.*, 2010; *Tao et al.*, 2011]. Highly anisotropic electron pitch angle distributions, which have a peak at 90° to the magnetic field, are called pancake distributions because of the way they appear in velocity space [*Wrenn et al.*, 1979].

There are two scientific communities, the ionospheric and magnetospheric, which deal with the theoretical description of diffuse auroral electron precipitation and its consequences. In the ionospheric community, several models of Earth's auroral electron transport have been developed, including a two-stream approach [*Banks et al.*, 1974], a multistream approach, which offers detailed pitch angle resolution [*Strickland et al.*, 1976], a numerical computation of the Boltzmann-Landau kinetic equation [*Khazanov*, 1979], a two-stream discrete ordinate approach [*Stamnes*, 1981], an application of a Feautrier solution [*Link*, 1992], a discrete ordinate technique [*Lummerzheim and Lilensten*, 1994], and a Monte Carlo technique [*Solomon*, 1993]. *Min et al.* [1993] applied the discrete ordinate approach of *Lummerzheim and Lilensten* [1994] and added small field-aligned ionospheric electric fields, allowing the study of ambipolar diffusion field influence on electron precipitation. *Peticolas and Lummerzheim* [2000] created a time-dependent electron transport model that simulates either flickering aurora or fast moving auroral filaments. However, all of the aforementioned approaches to auroral precipitation focus on superthermal electron (SE) transport at ionospheric altitudes in only one ionosphere, without taking into account the magnetically conjugate region.

The magnetospheric community focuses mostly on the processes that drive electron precipitation in the diffuse auroral region. As well known from literature, the source population for the diffuse aurora is plasma sheet electrons, with energies from hundreds of eV to 10 keV, which are scattered by resonant WPI into the loss cone [*Fontaine and Blanc*, 1983]. As mentioned above, it is also known that in this energy range both ECH and whistler mode chorus resonate with electrons [*Anderson and Maeda*, 1977] and both have thus been considered as mechanisms of electron precipitation from the plasma sheet. Their relative importance to driving the diffuse aurora still remains controversial and is a subject of much debate in the magnetospheric community [e.g., *Kennel et al.*, 1970; *Lyons*, 1974a; *Belmont et al.*, 1983; *Roeder and Koons*, 1989; *Horne and Thorne*, 2000; *Meredith et al.*, 2000; *Horne et al.*, 2003; *Meredith et al.*, 2009; *Thorne et al.*, 2010]. This paper will not attempt to argue what kind of waves, ECH or whistler mode chorus, are responsible for the scattering of plasma sheet electrons into the loss cone. They both contribute to diffuse aurora formation and they both can be relatively important, depending on their L shell location [*Ni et al.*, 2011a, 2011b; *Tao et al.*, 2011; *Zhang et al.*, 2015]. As this paper will show, WPI that drives precipitating fluxes in the region of diffuse aurora is only the first step in the formation of electron precipitation at ionospheric altitudes, which cannot be separated from the ionospheric calculation of electron flux degradation in the upper atmosphere via different kinds of collisional processes.

The majority of the theoretical electron precipitation studies in the ionospheric and magnetospheric communities that we have mentioned above have been basically disconnected. They are based on the assumption that the only source for the formation of such precipitation into the atmosphere-ionosphere system is pitch angle diffusion from the trapped zone to the loss cone. These studies do not consider the contribution of ionosphere-magnetosphere coupling (IM) processes in the formation of the electron distribution function at the ionosphere-magnetospheric boundary (700–800 km), which was recently studied for the first time by *Khazanov et al.* [2015a, 2015b]. Initial precipitation into the atmosphere is indeed, as typically discussed, the result of pitch angle scattering of plasma sheet electrons into the loss cone by different kinds of WPI processes. However, this is only the first step of the formation of the electron auroral precipitation at the upper ionospheric boundary; there is a second step that is missing from all previous theoretical studies of particle precipitation. As shown by *Khazanov et al.* [2014], depending on the energy spectra of the initial precipitation, about 15–40% of the energy of precipitated electrons returns back to the magnetosphere and conjugate ionospheric point of auroral magnetic field line. These returning SE fluxes experience additional degradation (energy cascade), secondary SE production, and reflection in the conjugate atmospheric region. This process can occur multiple times, causing electrons that go through multiple reflections to continuously lose their initial energy through the nonelastic collision processes of ionization and of excitation of neutral components of the ionosphere. Ionization leads to the production of secondary electrons ($E < 500–600$ eV) and, as a result, to the activation of lower energy SE spectra. The excitation of the neutral atmosphere also leads to an increase in the low-energy part of the electron spectra. Together with the secondary electron population, these SE participate in the heating of the plasma of ionosphere and magnetosphere via Coulomb collisions and their consequent trapping in the magnetosphere. These and other additional energy interchanges due to the SE population were discussed and calculated by *Khazanov et al.* [2014, 2015a, 2015b].

The precipitating electron spectral shape and differential fluxes in the diffuse aurora are very similar to those of the trapped plasma sheet electrons. A clearly defined relationship between the diffuse aurora and its particle source region was developed using observations of particles at geosynchronous orbit, observations of the auroral display, and observations of auroral electron precipitation around conjugate field lines, which was observed by DMSP 32, a polar-orbiting satellite, and presented by *Meng et al.* [1979]. In these observations of the diffuse aurora, electron differential fluxes and precipitating spectral shape was highly similar, sometimes even identical, to those of electrons that had been trapped in the plasma sheet and were simultaneously located at the conjugate magnetospheric equator. The characteristics of auroral electron precipitation are therefore determined by the features of particles in the conjugate magnetospheric equator, suggesting that the direct dumping of plasma sheet electrons is what produces the diffuse aurora. This characteristic similarity indirectly provides evidence for a lack of parallel electric fields in diffuse auroral regions. Diffuse electron precipitation is thus expected to occur simultaneously in both magnetically conjugate ionospheres.

As this paper will show, taking into account the diffuse auroral electron precipitation that is initially driven by WPI processes in the plasma sheet into both the magnetically conjugate ionospheric regions and the multiple reflections and degradation of these electrons in both conjugate atmospheres, increases the efficiency of the energy deposition of the electron diffuse aurora in the ionosphere-magnetosphere system. Compared to our previous recent studies of the formation of electron distribution function in the region of diffuse aurora [*Khazanov et al.*, 2014, 2015a, 2015b] we will now not be assuming the upper boundary conditions in the magnetically conjugated ionospheres at the altitude of 800 km. In this paper these boundary conditions represent a natural formation that occurs via WPI in the Earth's plasma sheet in combination with MI coupling processes, including at the altitude of 800 km where the ionospheric community typically uses these precipitated fluxes as artificially imposed boundary conditions.

This paper is organized into the following sections: the physical scenario and mathematical formalism of the simulations are described in section 2. Section 3 presents pitch angle scattering diffusion coefficient calculations by ECH waves and by whistler mode waves. All of our results are discussed in section 4, and finally, section 5 presents a summary and our conclusions.

2. Physical Scenario

The nonsteady state SuperThermal Electron Transport (STET) code, which we use for this study, was developed initially by *Khazanov et al.* [1992, 1993] for SE transport in the plasmasphere. The structure of this code, however, as well the idea of numerically implementing the kinetic electron equation in an inhomogeneous magnetic field, were based on the photoelectron transport code presented by *Khazanov* [1979] about 40 years ago. This code was generalized for further studies of ionosphere-magnetosphere coupling [*Khazanov et al.*, 1994; *Khazanov and Liemohn*, 1995] and global transport of SE [*Khazanov et al.*, 1996] as well as for the study of relativistic beam injections to space plasma [*Khazanov et al.*, 1999]. The STET model implements a full solution of the Boltzmann-Landau kinetic equation for the SE ionosphere-magnetosphere (I-M) coupling scenario, a solution which was derived by *Khazanov* [2011] and discussed in recent studies by *Khazanov et al.* [2014, 2015a, 2015b].

The SE I-M coupling problem, for electron energies $E > 1-2$ eV, starts with the Boltzmann-Landau kinetic equation presented by *Khazanov* [2011]. As we mentioned above, the dissipation processes for magnetospheric electrons in the diffuse aurora are affiliated with the cascading of high-energy electrons toward smaller energies and the production of secondary, tertiary, and further resultant electrons. Such ionization cascades can be treated with just a single kinetic equation, which includes all of the aforementioned processes [*Khazanov et al.*, 1994]. Following *Khazanov* [2011], this equation can be written as

$$\frac{1}{v}\frac{\partial \Phi}{\partial t} + \mu \frac{\partial \Phi}{\partial s} - \frac{1-\mu^2}{2}\left(\frac{1}{B}\frac{\partial B}{\partial s} - \frac{F}{E}\right)\frac{\partial \Phi}{\partial \mu} + EF\mu\frac{\partial}{\partial E}\left(\frac{\Phi}{E}\right) = Q + \langle S \rangle \tag{1}$$

where $\Phi = 2Ef/m^2$ is the SE flux, t is time, v is SE velocity, E is the particle energy; s is the distance along the field line, and μ is the cosine of the pitch angle. The geomagnetic field, B, includes inhomogeneities, and other forces, such as electric fields, are included in F. Q is the source term for SE, and $\langle S \rangle$ includes collisional integrals of SE interaction with neutral particles, thermal electrons, and ions, as well as WPI processes with different kinds of waves. All these terms are presented in Appendix A to this paper. The total gradient of thermal electron pressure is used to express the electric field in kinetic equation (1).

The STET code is nonsteady state (NSS) by nature, and this paper only presents the steady state result because the NSS calculation would require the time history of ECH, LBC, and UBC waves emissions, which is not available at this point. According to *Horne et al.* [2003], *Meredith et al.* [1999, 2009], *Li et al.* [2013], and *Zhang and Angelopoulos* [2014], ECH, LBC, and UBC waves emissions can last for several hours. In this case the formation of the electron distribution function in the energy range from tens of eV to several keV, the energy range of major focus in this paper, can be considered as a steady state process because it takes only several bounce periods [*Khazanov*, 2011] in the loss cone to reach the steady state condition for SE of these energies (see also *Khazanov et al.* [1993], *Khazanov and Liemohn* [1995], and *Khazanov et al.* [2012] for the specific details). Accordingly, all of our simulation results, which are presented in section 4, correspond to the steady state condition, and most of our results are presented at ionospheric altitudes that correspond to the loss/source cone.

It is useful to change variables in (1) from (μ, s) to (μ_0, s) in order to reduce unwanted effects associated with the approximation errors in numerical computation of the derivatives $\frac{\partial}{\partial s}$ and $\frac{\partial}{\partial \mu}$. This change of variables is given as

$$\mu_0 = \frac{\mu}{|\mu|}\sqrt{1 - \frac{B_0}{B}(1-\mu^2)} \tag{2}$$

with B_0 denoting magnetic field and μ_0 denoting the cosine of the pitch angle at the flux tube magnetic equator. This is a desirable change of variables because it changes μ to a slowly varying function of s (in the absence of external forces, μ_0 is simply the adiabatic invariant). Thus, approximation errors of numerical differentiation and their associated computation effects can be avoided (see *Khazanov* [2011] for details). Figure 1 represents the regions of the solution of kinetic equation (1) using different pitch angle variables connected by (2). The blue area on these plots corresponds to the loss cone region, and the regions with trapped electrons are shown in yellow, where lines illustrate the trajectory of bouncing particles.

The new variable μ_0 takes on values in the range $|\mu_{0_b}| < |\mu_0| < 1$, where the lower boundary $\mu_{0_b}(s) = \sqrt{1 - B_0/B(s)}$ is a function of s. The algorithm we use to solve kinetic equation (1) in the new variables (μ_0, s) has the specific feature that because the definition of μ_0 varies with s, the number of grid points in μ_0 also varies with s. In the magnetosphere, where magnetic field inhomogeneities cause s to vary significantly, the amount of steps in μ_0 is doubled for each step in s toward the magnetic equator. Figure 7.1 of the book by *Khazanov* [2011] illustrates this scheme by showing the adopted grid, presented as function of $\theta_0 = \cos^{-1}\mu_0$ and s.

Compared to our papers [*Khazanov et al.*, 2014, 2015a, 2015b] we are not setting our boundary conditions for the SE fluxes at the altitudes of 800 km in both conjugate ionospheric regions. In this paper the fluxes at 800 km form naturally based on WPI processes in the Earth's plasma sheet, as well as the multiple reflections and degradation of these electrons in both magnetically conjugated atmospheres.

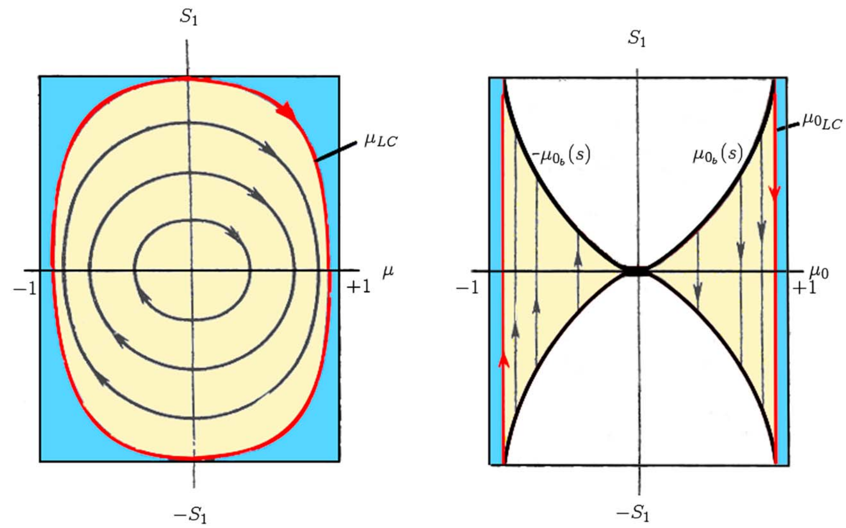

Figure 1. Regions where we solve the kinetic equation (1) using different pitch angle variables (left) μ and (right) μ_0, which are connected by equation (2). The blue region corresponds to the loss cone and the yellow region to the trapped zone, where lines illustrate the trajectory of bouncing particles. The loss cone/trapped zone boundary is shown in red.

Following numerical techniques presented by *Khazanov* [1979] and *Khazanov et al.* [1993, 1994], we solve kinetic equation (1) for the new variables (E, $\mu_0(\mu, s)$, s) under boundary conditions given as

$$\begin{aligned} \Phi(s = -s_1, \mu_0, E) &= \Psi^-(t, \mu_0, E) - 1 \le \mu_0 \le -\sqrt{1 - B_0/B(-s_1)} \\ \Phi(s = s_1, \mu_0, E) &= \Psi^+(t, \mu_0, E)\sqrt{1 - B_0/B(s_1)} \le \mu_0 \le 1 \end{aligned} \tag{3}$$

$$\Phi(s, \mu_0, E) = \Phi^{\text{trap}}(\mu_0, E) - \sqrt{1 - B_0/B(-s_1)} \le \mu_0 \le -\sqrt{1 - B_0/B(s)}\sqrt{1 - B_0/B(s)} \le \mu_0 \le \sqrt{1 - B_0/B(s_1)} \tag{4}$$

$$\frac{\partial\Phi(\theta_0 = 0, \pi)}{\partial\theta_0} = 0; \theta_0 = \cos^{-1}\mu_0 \tag{5}$$

$$\Phi^+(s, \mu_0 = \mu_{0_b}, E) = \Phi^-(s, \mu_0 = -\mu_{0_b}, E) \tag{6}$$

$$\frac{\partial\Phi^+}{\partial\theta_0}(s, \mu_0 = \mu_{0_b}, E) = -\frac{\partial\Phi^-}{\partial\theta_0}(s, \mu_0 = -\mu_{0_b}, E) \tag{7}$$

$$\Phi(s, \mu_0, E = E_{\text{max}}) = 0 \tag{8}$$

where $\Psi^{\pm}$ are lower altitude boundary conditions at 90 km, which were calculated from equation (1) for the condition of local equilibrium and θ_0 is the equatorial pitch angle.

Compared to all our previous work, we have introduced a new boundary condition (4) at the edge of the trapping zone (as shown in red in Figure 1 as μ_{LC} or $\mu_{0_{LC}}$, depending on pitch angle variables), for the energies $E \ge 600$ eV, because the main purpose of this paper is to predict electron precipitation into the diffuse auroral region, based on the trapped electron fluxes in the Earth's plasma sheet and their interaction with ECH, LBC, and UBC waves, which is presented in section 3. In this study, we assume that trapped electron fluxes, which are defined by (4), are isotropic and that their energy distribution is consistent with the typical Maxwellian-like energy distribution in the region of diffuse aurora [*Rees*, 1989]

$$\Phi^{\text{trap}}(E) = AEe^{-E/E_0} \tag{9}$$

where A is normalization factor and E_0 is the characteristic energy of the trapped plasma sheet electrons. We discuss the selection of these parameters in the section 4.

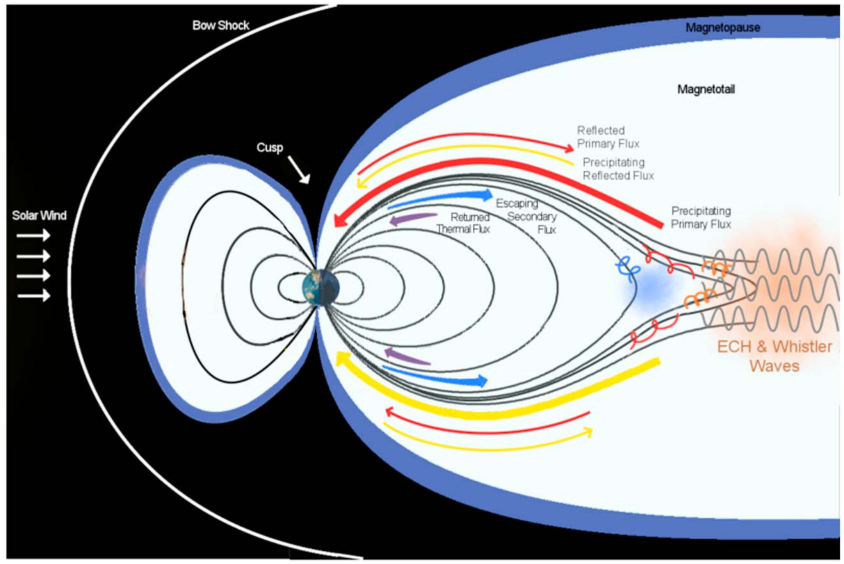

Figure 2. The physical scenario for this paper illustrating I-M exchange and WPI interaction processes. WPI (orange) causes primary precipitation (large red and yellow arrows) which can ionize the neutral atmosphere and produce secondary electrons. Secondary electron fluxes can also escape (blue) and precipitate into the conjugate region.

In the STET SE model, we use the following input: neutral thermospheric temperatures and densities are taken from the MSIS-90 model [*Hedin*, 1991], the ionospheric electron profile is calculated from the International Reference Ionosphere (IRI) model that [*Bilitza*, 1990] extended into the plasmasphere assuming that plasmasphere electron thermal density distribution varies in direct proportion to geomagnetic field as $n_e \sim B^a$, choosing a that is consistent with the calculation of $D_{\alpha\alpha}$ that we present in the following section.

We have calculated $D_{\alpha\alpha}$ at two radial distances: $L = 4.6$ and 6.8. For $L = 4.6$ we have used $n_e = 21.5$ cm^{-3} and $B_0 = 312$ nT, and for $L = 6.8$ we have used the values 12.0 cm^{-3} and 92.5 nT. The values of n_e and B_0 are based on the measurements by PWE (Plasma Wave Experiment), LEPA (Low Energy Plasma Analyzer), and the fluxgate magnetometer on board the CRRES spacecraft [*Meredith et al.*, 1999]. The parameter a is selected to be consistent with these values.

It should noted here that the selection of the thermal density structure in the ionosphere and plasmasphere is a very important element that strongly influences superthermal electron fluxes below the energies 10–20 eV. Here as in *Khazanov et al.* [2014], we use a density structure based on the IRI 90 model at ionospheric altitudes with modifications that have been introduced and extensively discussed by *Khazanov and Liemohn* [1995] using results suggested by *Buonsanto* [1989]. It is known that the usage of IRI 90 leads to large errors, particularly at high altitudes [e.g., *Buonsanto*, 1989; *Decker et al.*, 1997]. The cross sections for state-specific excitation, elastic collisions, and ionization were taken from *Solomon et al.* [1988]. All the calculations were performed for midnight local time, with $F10.7$ and $\langle F10.7 \rangle$ values of 150 and symmetric atmospheric conditions.

In this paper, the physical scenario and model are similar to that in *Khazanov et al.* [2015b] and are shown in Figure 2. An orange cloud indicates where precipitating electron fluxes are produced via WPI between plasma sheet electrons and ECH, LBC, and UBC waves. Hot electrons, with energies above 600 eV, are illustrated by tight orange spirals, and they are pitch angle scattered by the ECH and whistler waves drawn in gray. The hot electron fluxes were set up by (9) in the trapping zone region, as shown in Figure 1. The primary electrons, which precipitate symmetrically, enter the conjugate northern and southern ionospheres after being scattered into the loss cone, are indicated with yellow and red arrows labeled Precipitating Primary Flux, and come from the loss cone boundary conditions that have been described in Figure 1. Unlike our previous papers [*Khazanov et al.*, 2014, 2015a, 2015b] we calculate this precipitated flux at 800 km for the entire energy range of 1 eV and 10 KeV. Figure 2 also shows, with blue arrows, the secondary electron (SE) flux ($E < 600$ eV) that results from primary precipitation, which was calculated in the magnetosphere and both magnetically conjugated regions using the same method as in *Khazanov et al.* [2014, 2015a, 2015b]. The calculation, which is based on the solution of a single kinetic equation (1) with the collisional processes presented in Appendix A, includes the cascading of high-energy precipitated electrons from the magnetosphere toward small energies and the production of secondary, tertiary, and further resultant electrons. In Figure 2, blue spirals show particles that escape and move along magnetic field lines, some of which are trapped via Coulomb and WPI collisional processes. This trapped population is shown by a blue cloud.

As mentioned above, in this study the precipitated electron fluxes at 800 km form naturally via WPI processes in the Earth's plasma sheet in the combination with MI coupling processes. Also, the energy range for precipitated particles has been selected as 600–10,000 eV, a selection that does not have a principle effect here and simply has been chosen in order to be consistent with our previous studies by *Khazanov et al.* [2014, 2015a, 2015b] and to demonstrate the principle differences between some of the other theoretical approaches.

Section 4 of this paper will further describe this scenario and detail the contribution of different processes in the formation of electron distribution function in the region of the diffuse aurora.

3. Pitch Angle Diffusion in the Earth's Plasma Sheet

3.1. Wave Modes and Their Characteristics

A number of plasma waves have been observed in the Earth's magnetosphere. These include whistler mode chorus, plasmaspheric hiss, electrostatic cyclotron harmonics (ECH) emissions, ion cyclotron waves, and equatorial noise emissions. Among these the ECH and whistler mode chorus waves have received great attention due to their important role in pitch angle diffusion of plasma sheet electrons into the loss cone producing diffuse aurora.

ECH emissions are electrostatic emissions observed in bands between harmonics of the electron gyrofrequency, f_{ce}. ECH emissions are localized within a few degrees of the magnetic equator and are usually seen ~2100–0600 magnetic local time (MLT), the dawn and night regions, for $4 < L < 10$ [*Roeder and Koons*, 1989; *Meredith et al.*, 2009; *Ni et al.*, 2011a] and may even extend up to $L \approx 12$. ECH wave amplitudes are typically in the range 0.1–2.0 mV m^{-1} depending on substorm activity. In their model of plasma sheet electron interaction with ECH waves, *Zhang et al.* [2013] suggested that though their amplitude may be smaller than current detection levels, ECH waves may exist even beyond $\sim L = 12$. It is thought that ECH waves are driven by the loss cone instability of the ambient hot plasma sheet electron distribution in the presence of a low-density cold component [*Ashour-Abdalla and Kennel*, 1978; *Horne*, 1989; *Horne et al.*, 2003; *Tripathi et al.*, 2014a]. The harmonic bands are determined by cold electron density, which can be unstable. The first cyclotron harmonic band usually contains the major intensity of ECH wave power.

Chorus is an intense electromagnetic wave emission that propagates in the right-handed polarized whistler mode with frequency below f_{ce}. Whistler mode chorus waves are predominantly observed in the low-density region of the Earth's magnetosphere, outside the plasmasphere, over a wide distribution of magnetic local times (2200–1300 MLT). Distinct variations between nightside (2200–0600 MLT) and dayside (0600–1300 MLT) chorus have also been seen in observations. In particular, the majority of nightside chorus is confined to latitudes within 15° of the magnetic equator, while dayside chorus is able to propagate to much higher latitudes. Dayside chorus also typically propagates with wave normal angles larger than those of nightside chorus [*Li et al.*, 2009; *Ni et al.*, 2011b; *Meredith et al.*, 2012]. Chorus wave amplitudes range from more than ~100 pT during active times to well below 10 pT during quiet times. Whistler mode chorus waves are driven unstable by temperature anisotropies that cause linear growth at frequencies $\omega/\Omega_e \leq A/(1+A)$ where A is the temperature anisotropy given by $A = (T_\perp/T_{||}) - 1$, and $T_\perp$ ($T_{||}$) is the electron temperature in a direction perpendicular (parallel) to Earth's magnetic field [*Kennel and Petschek*, 1966] and $\Omega_e = 2\pi f_{ce}$. Several theories of nonlinear wave growth have also been developed to better understand chorus wave characteristics and generation processes [e.g., *Omura et al.*, 2009].

3.2. Electron Resonances

Scattering of plasma sheet electrons in the atmospheric loss cone is predominantly controlled by resonant interactions with plasma waves that are Doppler shifted in frequency to some integral multiple n of the electron cyclotron frequency. The resonance condition is expressed as

$$\omega - k_{||}v_{||} = n\Omega_{ce},\ n = 0, \pm 1, \pm 2, \cdots \tag{10}$$

where $k_{||}$ and $v_{||}$ are components of wave propagation vector and particle velocity along the ambient magnetic field. For parallel propagating chorus waves the dispersion relation is given by [*Stix*, 1962]

$$\left(\frac{k_{||}c}{\omega}\right)^2 = \frac{\omega_{pe}^2}{\omega\Omega_e}\frac{1}{(1-\omega/\Omega_e)} \tag{11}$$

where ω_{pe} is the electron plasma frequency and c is the velocity of light. Pitch angle diffusion by chorus waves is dominated by first-order cyclotron resonance. Using equations (10) and (11) the minimum energy for electrons which undergo first-order cyclotron resonance with parallel propagating chorus can be expressed as

$$E_{\min} = E_M\frac{\Omega_e}{\omega}(1-\omega/\Omega_e)^3 \tag{12}$$

where $E_M = B_0^2/8\pi n_c$, n_c is the cold electron density and B_0 is the ambient magnetic field. From equation (12) it is noted that lower frequency whistler mode waves resonate with higher-energy electrons, while higher-frequency waves resonate with lower energy electrons.

For ECH waves the wave vector has to be obtained by solving the hot plasma dispersion relation. The parallel wave vector ($k_{||}$) is estimated for a certain wave normal angle and then minimum resonant energy is calculated using equation (10). For electrostatic waves hot plasma dispersion relation is given by

$$\epsilon(\omega,k) = 1 - \frac{\omega_{pe}^2}{k^2}\sum_{n=-\infty}^{\infty}\int \mathrm{d}v\frac{J_n^2[k_\perp v_\perp/\Omega_e]}{k_{||}v_{||}-\omega-n\Omega_e}\times\left[\frac{n\Omega_e}{v_\perp}\frac{\partial F}{\partial v_\perp}+k_{||}\frac{\partial F}{\partial v_{||}}\right] \tag{13}$$

Here J_n is the Bessel function of order n and F is the electron distribution function. For a Maxwellian plasma, assuming $k_\perp >> k_{||}$, equation (13) becomes

$$1 = \frac{2\omega_{pe}^2}{\lambda}\sum_{n=1}^{\infty}e^{-\lambda}I_n(\lambda)\frac{n^2}{\omega^2-n^2\Omega_e^2} \tag{14}$$

where $I_n(\lambda)$ are the modified Bessel functions with $\lambda = \frac{T_c k^2}{m_e\Omega_e^2}$, T_c is the cold electron temperature, and m_e the mass of electron.

Ronnmark et al. [1978] have given solution of equation (13) for a three-component model distribution function with $B_0 = 158$ nT [*Ronnmark et al.*, 1978, Figures 2 and 6]. We use this solution to illustrate the calculation of resonant energy of ECH waves. For wave normal angle 89°, $k_{||}$ is found to be 4.8×10^{-6} cm^{-1} and 8.8×10^{-6} cm^{-1} for $\omega(=\omega/\Omega_e) = 1.6$ and 1.3, respectively. Substituting these values in equation (10) and using $n = 1$, we obtain the minimum resonant energies 3.4 keV and 259 eV for$\omega = 1.6$ and 1.3, respectively, whereas for $n = 2$, the corresponding energy values are 1.5 keV and 1.4 keV. It may now be noted that these values of $k_{||}$ do not change in the solution of dispersion relation of a Maxwellian plasma for the model distribution function used by *Ronnmark et al.* [1978]. Further, *Tripathi and Singhal* [2005] have solved equation (14) for a somewhat different set of plasma parameters and a different magnetic field (B_0). It is found that the $k_{||}$ values are not too different. Thus, in the present study, minimum resonant energies for ECH waves will differ from the values mentioned above by approximately 4 times for $L = 4.6$ ($B_0 = 312$ nT) and about 1/3 for $L = 6.8$ ($B_0 = 92.5$ nT). These estimates are obtained using the solution of parallel wave vector from *Ronnmark et al.* [1978]. Also, lower values of resonant energy will be obtained for lower values of the wave normal angle.

3.3. Diffusion Coefficient for ECH Waves

The pitch angle diffusion coefficient for electrostatic ECH waves, in units of per second, is given by *Lyons* [1974a],

$$D_{\alpha\alpha} = \sum_{n=-\infty}^{\infty}\int k_\perp \mathrm{d}k_\perp\left[\psi_{n,k}\left(\frac{(n\Omega_e/\omega_k)-\sin^2\alpha}{\sin\alpha\cos\alpha}\right)^2\right]_{k_{\|}=k_{\|\mathrm{res}}} \tag{15}$$

where

$$\psi_{n,k} = \frac{e^2}{4\pi m_e^2}\frac{|E_k|^2}{V}\left(\frac{\omega_k}{|k|}\right)^2\frac{J_n^2(k_\perp v_\perp/\Omega_e)}{v^4|v_\| - \partial\omega_k/\partial k_\||}$$

and $k_\perp$ and $k_\|$ are the components of the wave vector perpendicular and parallel to the ambient magnetic field B_0, respectively, $k_{\|\mathrm{res}} = (\omega_k - n\Omega_e)/v_\|$, $\Omega_e = |eB_0/m_e|$ is the (angular) electron gyrofrequency, E_k is wave electric field at each k, ω_k is wave frequency as a function of k, and v and α are, respectively, particle velocity

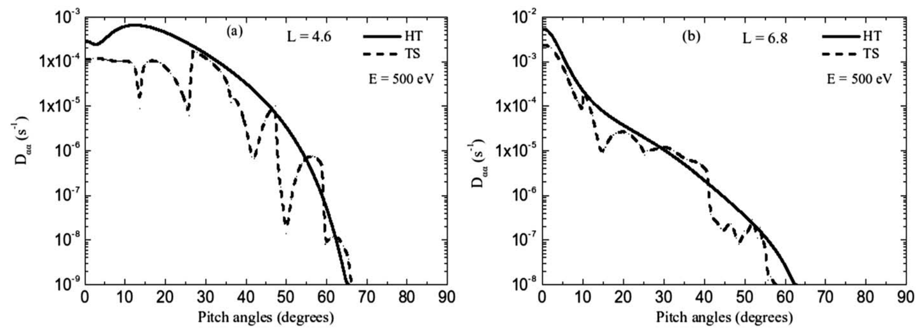

Figure 3. ECH wave diffusion coefficients $D_{\alpha\alpha}$ calculated using the approach of HT (solid lines) and TS (dashed lines) at two radial distances: (a) $L = 4.6$ and (b) $L = 6.8$ for electrons of energy 500 eV. There is general agreement (except bumps) between the two approaches.

and pitch angle. V indicates the plasma volume, e/m_e the electron charge to mass ratio, and $J_n$the Bessel function of order n. In the work of *Horne and Thorne* [2000] [also *Ni et al.*, 2011a] the electric field spectrum is assumed to have the form

$$|E_k|^2 = Ak_\perp^2 \exp\left[-\left(\frac{k_\perp}{k_{\perp_0}}\right)^2\right]\left\{\exp\left[-\left(\frac{k_{||}-k_{||_0}}{\Delta k_{||}}\right)^2\right] + \left[-\left(\frac{k_{||}+k_{||_0}}{\Delta k_{||}}\right)^2\right]\right\} \quad (16)$$

where $A = \frac{4\pi^{3/2}}{k_{\perp_0}^4 \Delta k_{||}} V|E_W|^2$ is the normalization constant. *Tripathi and Singhal* [2009] express

$$|E_k|^2 = [V/N(\omega)]E^2(\omega)g_\omega(\theta) \quad (17)$$

where $N(\omega)$ is a normalization factor [*Lyons*, 1974b]

$$N(w) = 2/2\pi^2 \int_1^0 g_\omega(\cos^{-1}x)k_\perp \left|J\left(\frac{k_\perp, k_{||}}{\omega, x}\right)\right| \mathrm{d}x \quad (18)$$

Here $E^2(\omega)$ is the square of wave electric field per unit frequency and $g_\omega(\theta)$ gives the distribution of wave energy with wave normal angle θ (angle between B_0 and k), $x = \cos\theta$, and $J\left(\frac{k_\perp, k_{||}}{\omega, x}\right)$ is the Jacobian of the transformation.

3.4. Diffusion Coefficients for Whistler Mode Waves

To calculate the diffusion coefficient ($D_{\alpha\alpha}$) for whistler mode waves, we have used the expression of $D_{\alpha\alpha}$ given by *Lyons* [1974b] [also *Singhal and Tripathi*, 2006; *Tripathi et al.*, 2014b]

$$D_{\alpha\alpha} = \sum_{n=-\infty}^{\infty} \int_0^{x_{\max}} x\mathrm{d}x D_{\alpha\alpha}^{nx} \quad (19)$$

where $x = \tan\theta$ and $D_{\alpha\alpha}^{nx}$ is given by

$$D_{\alpha\alpha}^{nx} = \left.\frac{\pi\cos^5\theta\Omega_e\left(-\sin^2\alpha - n\Omega_e/\omega_k\right)^2|\phi_{n,k}|^2}{2C_1\psi^{3/2}|1+n\Omega_e/\omega_k|^3 I(\omega_k)} \times f(\omega)g_\omega(x)\left(1 - \frac{1}{v_{||}}\left.\frac{\partial\omega_k}{\partial k_{||}}\right|_x\right)\right|_{\left(\frac{\omega_k}{\Omega_e}\right) = \left(\frac{\omega_k}{\Omega_e}\right)_{\mathrm{res}}} \quad (20)$$

where $f(\omega)$ is the wave magnetic field spectral density and $g_\omega(x)$ gives the wave normal distribution, $C_1 = \int f(\omega)\mathrm{d}\omega$. Expressions for $|\phi_{n,k}|^2, I(\omega_k), \psi$, and $\left.\frac{\partial\omega_k}{\partial k_{||}}\right|_x$ are obtained using the dispersion relation for cold plasma waves [*Stix*, 1962] under the high-density approximation ($(\omega_{\mathrm{pe}}/\Omega_e)^2 \gg \omega/\Omega_e$) [*Lyons*, 1974b; *Singhal and Tripathi*, 2006]. This high-density approximation was also used by *Su et al.* [2009, 2010]. *Ni et al.* [2008], *Shprits and Ni* [2009], and *Ni et al.* [2011b] calculated the diffusion coefficient using the Full Diffusion Code in a manner similar to that of *Glauert and Horne* [2005]. The Full Diffusion Code uses the full electromagnetic dispersion relation for cold magnetized plasma, so it can address any ratio of plasma to cyclotron frequency, $\omega_{\mathrm{pe}}/\Omega_e$.

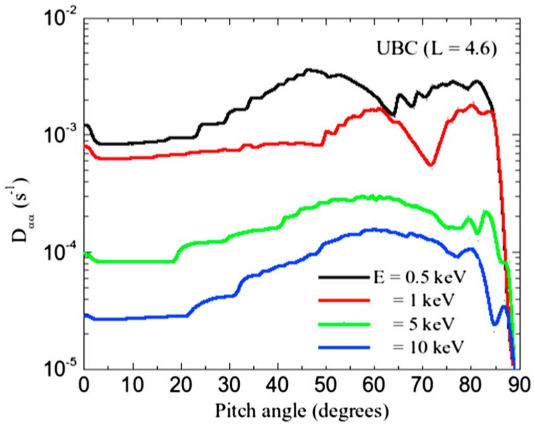

Figure 4. Pitch angle diffusion coefficients $D_{\alpha\alpha}$ as a function of pitch angle for UBC waves at $L = 4.6$ for four different energy values.

3.5. Approaches and Comparison

For diffusion coefficients of ECH waves the use of equation (16) based on *Horne and Thorne* [2000] produces smooth $D_{\alpha\alpha}$ profile, while using equations (17) and (18) expressed by *Tripathi and Singhal* [2009] produces bumps in the calculation of $D_{\alpha\alpha}$ profile. In Figure 3 we have compared the $D_{\alpha\alpha}$ calculations using the approach of *Horne and Thorne* [2000, HT] and *Tripathi and Singhal* [2009, TS] at two radial distances: (a) $L = 4.6$ and (b) $L = 6.8$ for electron energy 500 eV. It may be noted that there is general agreement (except bumps) between the both approaches.

In the present work, the calculated values of ratio ω_{pe}/Ω_e are 4.8 and 12.0 for $L = 4.6$ and 6.8, respectively. Therefore, the high-density approximation is applicable. In Figures 4 and 5, we present pitch angle diffusion coefficients for upper band and lower band whistler mode chorus waves, respectively, at $L = 4.6$ for four energy values (0.5, 1.0, 5.0, and 10.0 keV). In Figures 6 and 7 the diffusion coefficients are plotted for $L = 6.8$. It may be noted from Figures 5 and 7 for LBC that the diffusion coefficients for $L = 4.6$ are negligible at electron energies < 5 keV, while for $L = 6.8$ the values of $D_{\alpha\alpha}$ for LBC are appreciable at these lower energies. This behavior of $D_{\alpha\alpha}$ is due to lower resonant energies for $L = 6.8$ as compared to those for $L = 4.6$. Resonant energies for whistler mode waves are controlled by magnetic energy per particle, E_M. The values of E_M are 1.8 keV and 11 keV corresponding to $L = 6.8$ and 4.6, respectively. The calculated diffusion coefficients for whistler mode chorus waves in the present work are generally in agreement with the values reported in the works of *Su et al.* [2009, 2010] and *Ni et al.* [2011b].

3.6. Waves and Plasma Parameters

For calculation of $D_{\alpha\alpha}$ for ECH and whistler mode waves, we have used the temporal growth rate profiles to represent the wave spectral density distribution. *Tripathi et al.* [2013] have solved the dispersion relation for parallel propagating *R* mode waves using a two-component electron distribution function: a cold component assumed to be isotropic and Maxwellian, and a hot component that is anisotropic with temperature anisotropy *A*. It is found that as the anisotropy is increased, the whistler temporal growth rate increases and shifts toward higher frequencies.

Calculations were performed for two values, $A = 1.1$ and 6.0. For anisotropy $A = 1.1$ the temporal growth rate profile of whistler mode waves covers the normalized frequency range $\omega \approx 0.1-0.5$, having peaks at 0.43 and 0.30 corresponding to $L = 4.6$ and 6.8, respectively. The anisotropy $A = 6.0$ produces the waves in the ranges of $\sim$0.4–0.8 and $\sim$0.2–0.75 having peaks at 0.61 and 0.65 for $L = 4.6$ and 6.8, respectively. Gaussian fits have also been applied to temporal growth rate profiles. For $A = 1.1$ the frequency range of Gaussian fits are $\approx$ 0.25–0.5 and $\approx$ 0.1–0.5 for $L = 4.6$ and 6.8, respectively. For $A = 6.0$, the ranges are $\approx$ 0.4–0.8 and $\approx$ 0.4–0.75 for $L = 4.6$ and 6.8 respectively. We have used the profiles for A = 1.1 to represent LBC, whereas the profiles for $A = 6.0$ represent UBC. For LBC and UBC waves the $D_{\alpha\alpha}$ calculated for temporal and Gaussian profiles are very close. The magnetic field amplitude for LBC and UBC waves are taken to be 10 pT and for ECH waves a value of 1 mV m^{-1} is used.

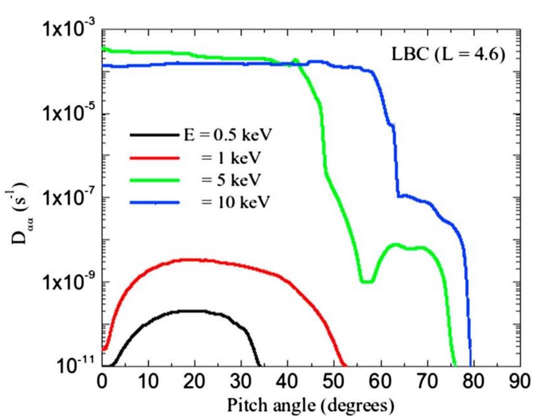

Figure 5. Pitch angle diffusion coefficients $D_{\alpha\alpha}$ as a function of pitch angle for LBC waves at $L = 4.6$ for four different energy values.

The Plasma Wave Experiment on board the Combined Release and Radiation Effects

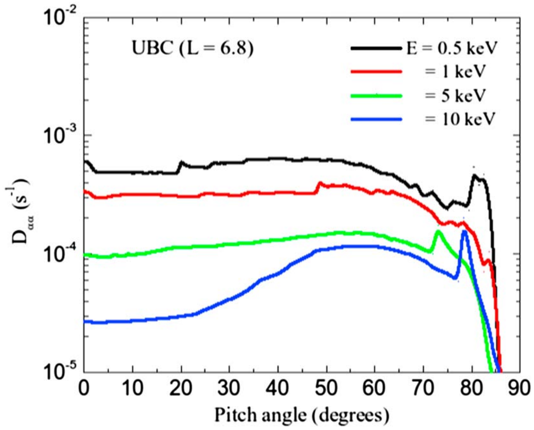

Figure 6. Pitch angle diffusion coefficients $D_{\alpha\alpha}$ as a function of pitch angle for UBC waves at L = 6.8 for four different energy values.

Satellite (CRRES) provided a good wave database for ECH, LBC, and UBC [*Meredith et al.*, 2009]. ECH wave electric field amplitude in the first harmonic band is obtained in the range 0.2–2.0 mV m^{-1} depending on geomagnetic activity levels. For chorus waves, the wave magnetic field intensities are obtained from the measured electric field intensities assuming parallel propagation. Magnetic field amplitude for LBC waves varies from 10 pT (quiet conditions) to 60 pT (active conditions). For UBC waves the values are 5 pT and 45 pT, respectively. The wave amplitudes assumed in the present work are within the range of the observed data set.

Furthermore, LBC waves are assumed to be confined within ±15° of the magnetic equator, whereas UBC and ECH waves are confined within ±10° and ±3°, respectively [*Ni et al.*, 2011a, 2011b]. Calculations have been performed at two shells, L = 4.6 and 6.8, having the same plasma parameters as used by *Tripathi et al.* [2013]. These physical parameters are for $L = 4.6$: $n_c = 21.5$ cm^{-3}, $T_c = 4$ eV, and $B_0 = 312$ nT and for $L = 6.8$: $n_c = 12.0$ cm^{-3}, $T_c = 10$ eV, and $B_0 = 92.5$ nT. In the present study we have used wave properties based on calculated temporal growth rate profiles assuming a certain amplitude for waves. However, in our future studies, we plan to use observation-based wave properties in modeling the wave scattering effect.

4. Results and Discussion

Using the SE model for the conditions described above, we now demonstrate our SE flux calculation in the region of the electron diffuse aurora, with an emphasis on the ionosphere-magnetosphere coupling processes and energy and particle flux redistribution between the magnetosphere and two magnetically conjugate ionospheres. As mentioned above, the main purpose of this paper is to predict electron precipitation into the region of the diffuse aurora based on the content of trapped electron fluxes in the Earth's plasma sheet, and the electron interaction with ECH, LBC, and UBC wave activity that has been described in section 3. In order to do this, we have introduced the new boundary condition (4) at the edge of the trap zone, for energies $E \geq 600$ eV. The trapped electron fluxes, defined by (9), are isotropic, and their energy distribution is consistent with the typical Maxwellian-like energy distribution in the diffuse auroral region [*Rees*, 1989], $\sim AEe^{-E/E_0}$. This paper assumes that trapped plasma sheet electrons have energies in the range of 600 eV–10 KeV, an assumption consistent with our previous SE studies in diffuse auroral regions [*Khazanov et al.*, 2014, 2015a, 2015b]. We have chosen in (9) $A = 10^3$ and $E_0 = 1$ KeV, and we assume these parameters to be the same at the L shells 4.6 and 6.8, which will be our major focus. Our selection of these parameters leads to total omnidirectional plasma sheet fluxes of 10^9 cm^{-2} s^{-1}, a number consistent with previous measurements at $L \sim 17$ by *Bame et al.* [1967] and at geosynchronous orbit by *Moore and Arnoldy* [1982] and very recent measurements by *Runov et al.* [2015].

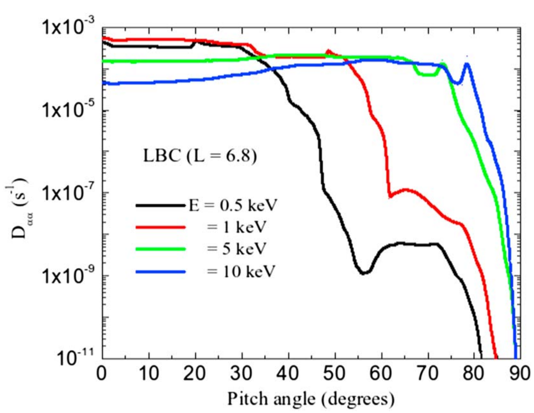

Figure 7. Pitch angle diffusion coefficients $D_{\alpha\alpha}$ as a function of pitch angle for LBC waves at L = 6.8 for four different energy values.

The numerical approach that has been outlined in section 2 allows the calculation of SE fluxes with energies below 600 eV in the entire simulation domain, which is shown as blue

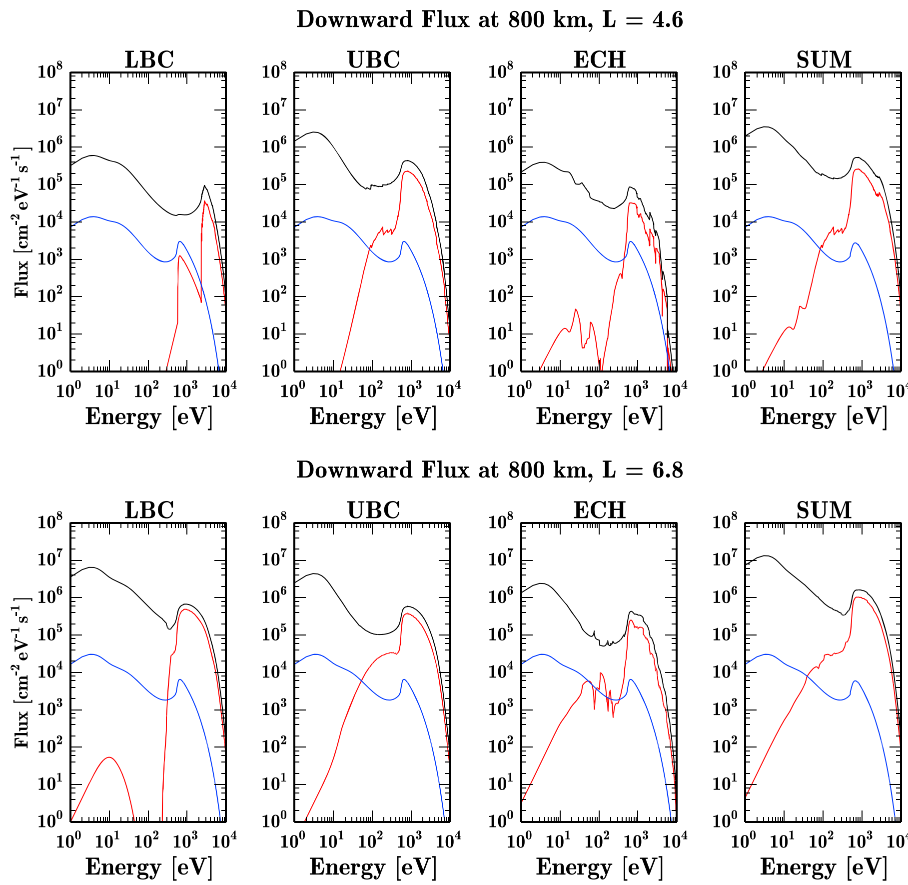

Figure 8. Downward directional electron flux from 1 eV to 10 keV at 800 km for (top row) $L = 4.6$ and (bottom row) $L = 6.8$ calculated for three types of WPI: (first column) LBC, (second column) UBC, (third column) ECH, and (fourth column) their SUM. Calculations for three scenarios are included the complete simulation (black), no MI coupling (red), and no wave activity (blue).

and yellow in Figure 1, as well as the calculation in both magnetically conjugated atmospheric regions. However, for energies between 600 eV and 10 KeV, this approach only includes the processes of electron scattering from the trapped zone (yellow region) into the loss cone area (blue region) and the multiple reflection and degradation into both magnetically conjugate ionospheres following initial precipitation. Because we impose the boundary condition (4) above 600 eV, the code neglects the communication of these higher-energy electrons with the trapped zone as they travel back from the magnetically conjugate regions through the loss cone.

We first present, in Figure 8, the calculated downward directional electron flux distribution at 800 km for different limiting cases. Figure 8 (top and bottom rows) shows electron flux formation at $L = 4.6$ and $L = 6.8$, respectively. The first three windows in each row illustrate the relative role of each wave—LBC, UBC, and ECH—in the formation of electron precipitation, and the forth window in each row, entitled SUM, shows precipitated electron fluxes that includes all three types of wave activity. Here black lines represent a scenario of complete simulation using the new boundary conditions (4) and (9), as described in section 2. Blue lines correspond to the case when wave activity is “turned off” in the STET code, and plasma sheet electrons are scattered into the loss cone solely via Coulomb collisions. Red lines indicate precipitated electron fluxes at 800 km when both WPI and Coulomb collision processes move plasma sheet electrons into the upper ionospheric region, but both magnetically conjugate ionospheric regions are completely disconnected, and there is no communication at all between magnetospheric and ionospheric processes. This case represents the major focus of most studies in the magnetospheric community, which, as described in the section 1, emphasizes the relative contribution of different kinds of waves that drive plasma sheet electrons into the loss cone.

In each window of Figure 8, the sharp behavior of fluxes at 600 eV is a result of setting the boundary condition at the edge of the trap zone, which is imposed for each case from 600 eV to 10 keV, and in each case, the charactertistic Maxwellian shape of the initially precipitating primary distribution is visible.

The differences between the different types of waves and between $L = 4.6$ and $L = 6.8$ can be explained by the $D_{\alpha\alpha}$ behavior at different L shells, as presented in Figures 3–7. From Figure 3 of $D_{\alpha\alpha}$ for ECH waves it may be noted that $D_{\alpha\alpha}$ at $L = 6.8$ is much greater than $D_{\alpha\alpha}$ at $L = 4.6$. This behavior of $D_{\alpha\alpha}$ is reflected in Figure 8 (third column) in the black line (complete simulation) and the blue line (no wave activity). $D_{\alpha\alpha}$ for UBC at $L = 4.6$ and 6.8 are comparable for electron energies > 1 keV. For lower energies $D_{\alpha\alpha}$ at $L = 4.6$ is greater than $D_{\alpha\alpha}$ at $L = 6.8$ (Figures 4 and 6).This is reflected in black and blue lines in Figure 8 (second column). Finally, $D_{\alpha\alpha}$ for LBC is much larger for $L = 6.8$ than for $L = 4.6$ as may be noted in Figures 5 and 7. Therefore the downward flux shown in Figure 8 (first column)is much greater for $L = 6.8$ than for $L = 4.6$ in the complete simulation (black line).

In Figure 8, the differences between $L = 6.8$ and $L = 4.6$ are also due to the fact that the pitch angle diffusion coefficients, which increase near the $L = 6.8$ loss cone boundary, give escaping ionospheric secondary electrons an additional push toward the trapped zone. These differences also owe to growth of pitch angle diffusion with increasing L shell, as discussed by *Khazanov et al.* [2013, 2015b].

Figure 8 illustrates that wave activity greatly contributes to the formation of SE fluxes via the scattering of plasma sheet electrons into the loss cone, compared to the case when only Coulomb collisional processes (blue lines) are taken into account. Both the cases illustrated in Figure 8 by black and blue lines correspond to scenarios when MI coupling processes, including the subsequent interaction of primary electrons with the neutral and charged particles in both magnetically conjugated ionospheres, and the affiliated production of secondary electrons ($E < 600$ eV) are included. Omitting these MI coupling processes completely (case shown in red lines) causes a dramatic difference in the calculated flux for energies below 600 eV, even when Coulomb collisions are the only mechanism for plasma sheet electron scattering.

The difference between the example cases shown in black and red presented in Figure 8 clearly demonstrate the importance of including MI coupling processes. As shown by *Khazanov et al.* [2014], depending on the energy spectra of the initial precipitation, about 15–40% of the energy of precipitated electrons returns back to the magnetosphere and to the conjugate ionospheric point along the auroral magnetic field line. These returning SE fluxes experience additional degradation (energy cascade), secondary SE production, and reflection in the conjugate atmospheric region. This process can occur multiple times, causing electrons that go through multiple reflections to continuously lose their initial energy through the nonelastic collision processes of ionization and of excitation of the neutral components of the ionosphere. Ionization leads to the production of secondary electrons ($E < 600$ eV) and, as a result, to the activation of lower energy SE spectra. The excitation of the neutral atmosphere also leads to the increase of the low-energy part of the electron spectra. Together with the secondary electron population, these SE participate in the heating of the plasma of ionosphere and magnetosphere via Coulomb collisions and their consequent trapping in the magnetosphere.

These and other additional energy interchanges due to the SE population were discussed and calculated by *Khazanov et al.* [2014, 2015a, 2015b], and the results that are shown in Figure 8 and that will be presented below in Figures 9–14 confirm these initial studies and provide another indication of the self-consistency of our studies. In our current study, we do not set up the atmospheric fluxes precipitating at the upper ionospheric boundary; we instead calculate these fluxes based on the logic of WPI processes in the Earth's plasma sheet, as well as the MI coupling phenomena that involves the two magnetically conjugated diffuse auroral regions.

Along with Figure 8, we present Histogram 1, which includes downward particle fluxes (Figure 15, left) and energy fluxes (Figure 15, right) at the altitude of 800 km integrated over the entire energy range of 1 eV–10 keV for the same example cases shown in Figure 8. These fluxes are presented for both $L = 4.6$ (dashed bars) and $L = 6.8$ (solid bars) and include all types of wave activity, just as in the SUM window of Figure 8. The gray, red, and blue colors in Histogram 1 correspond to the cases shown in black, red, and blue in Figure 8: the complete simulation with all processes included (gray), the simulation with no MI coupling (red), and with no wave activity and only Coulomb collisional processes (blue).

Histogram 1 illustrates again that the total particle and energy fluxes for both $L = 4.6$ and $L = 6.8$ are significantly increased in the complete simulation, which includes wave activity and MI coupling. In addition

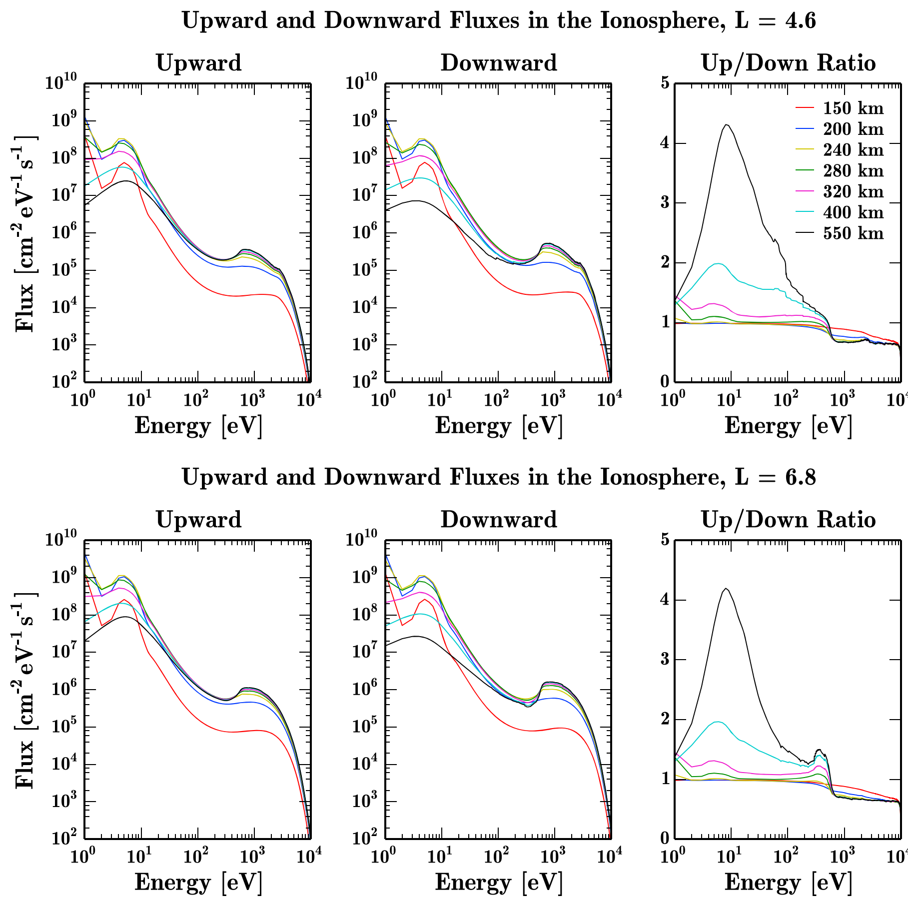

Figure 9. (first column) Upward and (second wind) downward electron fluxes from 1 eV to 10 keV at (top row) $L = 4.6$ and (bottom row) $L = 6.8$ for ionospheric altitudes between 150 and 550 km. (third column) The ratio of upward to downward fluxes is also presented. Upward fluxes dominate for $E < 600$ eV, while downward fluxes dominate for $E \geq 600$ eV.

to the cases of Figure 8, Histogram 1 also presents the total downward SE flux (green bar), which is integrated over the SE energy range of 1–600 eV, emphasizing that the flux enhancement in our new full simulation also includes a significant flux enhancement in the SE range.

Next, Figure 9 displays upward and downward electron fluxes at $L = 4.6$ (top row) and $L = 6.8$ (bottom row) for ionospheric altitudes between 150 km and 550 km. The first window in each row corresponds to upward fluxes and the second window to downward fluxes. The differences between these two fluxes are shown in the corresponding windows, entitled Up/Down Ratio. For both L shells, upward fluxes dominate for the energies below 600 eV and show clear differences, in Figure 9 (third column), from downward fluxes above the altitude of approximately 240 km, while the downward fluxes always dominate for energies above 600 eV.

In this high-energy range, as discussed in *Khazanov et al.* [2014, 2015b], the domination by fluxes down results from ionospheric degradation of primary electrons. Upward secondary electron fluxes in the range $E < 600$ eV are greater than the precipitating flux because downward secondary fluxes have undergone trapping and scattering during their multiple reflections through the plasmasphere after they are produced in the conjugate ionosphere. Consequently, these fluxes undergo low-energy degradation and have a lower intensity than the escaping secondary fluxes, which result directly from WPI. The fluxes approach each other at lower altitudes, as seen in Figure 9 (third column), due to flux isotropization via elastic collisions with neutral particles.

Figure 10 displays omnidirectional SE fluxes in the ionosphere, calculated for exactly the same conditions as the fluxes Figure 9, and is presented in a similar format, with separate windows for $L = 4.6$ and $L = 6.8$.

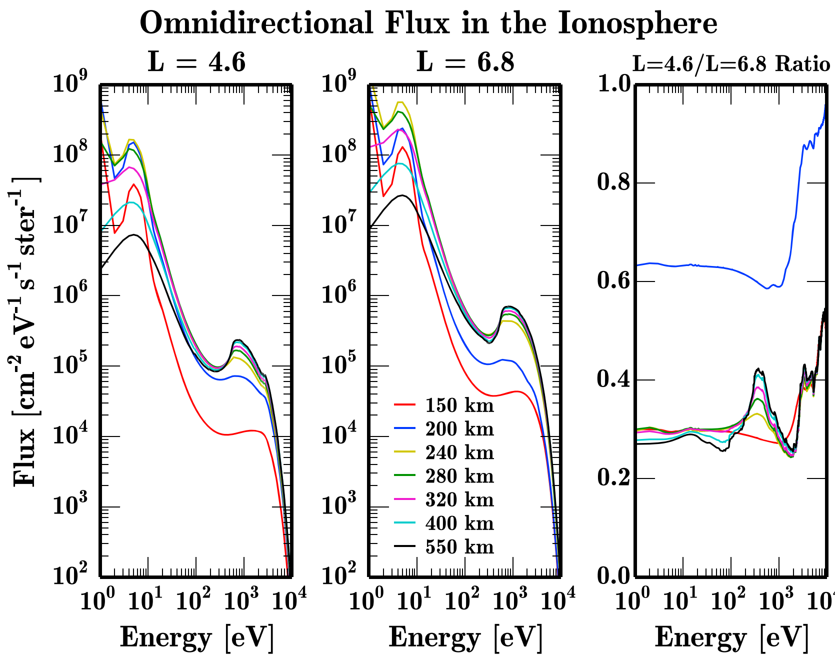

Figure 10. Omnidirectional electron fluxes from 1 eV to 10 keV at (left) $L = 4.6$ and (middle) $L = 6.8$ for ionospheric altitudes between 150 and 550 km. (right) The ratio of $L = 4.6$ to $L = 6.8$ is also presented, which indicates that electron precipitation is stronger at $L = 6.8$, due to the greater efficiency of WPI processes at larger distances.

Figure 10 (right) shows the ratios of omnidirectional fluxes at different L shells and indicates that electron precipitation is stronger at $L = 6.8$, an effect due to greater efficiency of WPI processes at larger distances.

For both directional flux (shown Figure 9) and omnidirectional flux (shown in Figure 10), the spectra of the secondary electrons ($E < 600$ eV) have distinctly recognizable features at 150 km and 240 km. The loss of secondary electrons during the excitation of N_2 vibrational levels causes a trough between 2 and 3 eV, which disappears at altitudes above 250–300 km, where collisional processes between electrons and neutral particles are dominated by Coulomb collisional processes.

While Figures 8–10 present electron flux as a function of energy, it is also important to consider the total upward and downward particle and energy fluxes in the ionosphere integrated over the entire energy domain of 1 eV–10 KeV. These integrated total fluxes are presented in Figure 11, which shows the same three exemplary cases described in Figure 8, again at $L = 4.8$ and $L = 6.8$. Comparing the scenarios with WPI and/or Coulomb collisions, shown again in black and blue, to the scenario with MI coupling processes completely omitted (red lines), demonstrates the dramatic differences in the calculated integrated particle and energy fluxes as a function of altitude.

The limiting cases that we show in Figure 11—as in Figure 8, where we showed only SE energy spectra—clearly demonstrate that the formation of the auroral electron precipitation at the ionospheric boundary is due to MI coupling processes, as well as different types of WPI and Coulomb collisional processes. During this coupling along the auroral magnetic field line, returning SE fluxes experience additional degradation (energy cascade), secondary SE production, and reflection in the conjugate atmospheric region, a process can occur multiple times, causing electrons that go through multiple reflections to continuously lose their initial energy through the nonelastic collision processes of ionization and of excitation of the neutral components of the ionosphere.

Table 1 further demonstrates the influence of MI coupling processes on the formation of total particle and energy SE fluxes in the upper ionosphere at 800 km and shows the partial contribution of each wave in the formation of energy and particle fluxes. Table 1 indicates that the majority of both the upward and downward particle and energy flux contribution comes from UBC, which contribute between 50 and 70% of the flux. The LBC and ECH waves for $L = 4.6$ only contribute about 20–40% and 5–10% of the flux, respectively. However, at $L = 6.8$, the LBC contributes the majority, about 45–50% of the flux, with UBC contributing ∼35% and

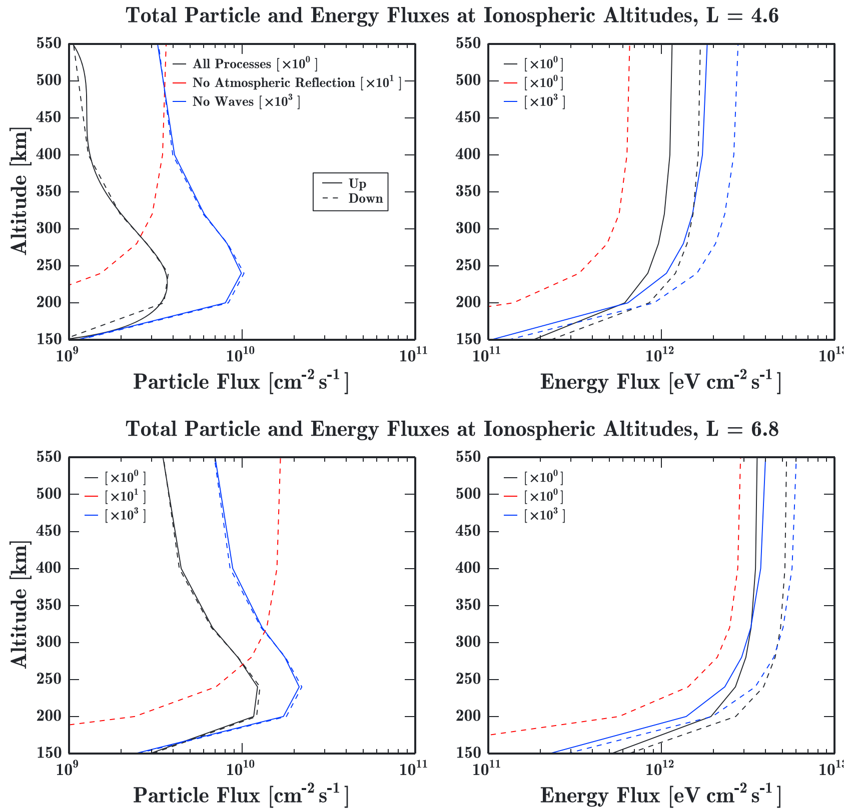

Figure 11. Upward (solid lines) and downward (dashed lines) (left column) particle flux and (right column) energy flux integrated from 1 eV to 10 keV for altitudes between 150 and 550 km. Calculations for three scenarios are included the complete simulation (black), no MI coupling (red), and no wave activity (blue). Fluxes are scaled as indicated in the legend.

ECH, as at $L = 4.6$, contributing the least, about 10–20% of the flux. These values are consistent with the $D_{\alpha\alpha}$ calculations presented in Figures 3–7. At $L = 4.6$, $D_{\alpha\alpha}$ for UBC waves is largest followed by LBC and ECH waves as can be seen from Figures 4, 5, and 3 a, respectively. However, at $L = 6.8$, $D_{\alpha\alpha}$ for LBC waves is largest followed by UBC as illustrated in Figures 6 and 7. $D_{\alpha\alpha}$ for ECH waves, although comparable near the loss cone, drops with pitch angle much faster (Figure 3b) than UBC and LBC waves.

Now, we move to the magnetosphere, and present the energy distribution of SE for different pitch angles at $L = 4.6$ and $L = 6.84$ in the region of the geomagnetic equator. Figure 12 shows these distributions for the pitch angles 0° and 5°, and Figure 13 for 70° and 90°, respectively. The organization of Figures 12 and 13 follows that of Figure 8 and includes different limited cases of the STET runs as well as the partial contribution of LBC, UBC, and ECH waves in the formation of SE energy fluxes for the selected pitch angles in the magnetosphere.

All calculations that are shown in Figures 12 and 13 correspond to the wave activity and plasma parameters that have been discussed in section 3, and these figures again demonstrate the comparison, described above, between the importance of WPI, Coulomb collisional, and MI coupling processes. The solid lines in these figures correspond to $L = 4.6$, and the dashed lines to $L = 6.8$.

The SE energy fluxes presented in Figure 12 correspond to the two pitch angles 0° and 5°. Particles with 0° pitch angles are in the loss cone, and particles with a 5° pitch angle, for both $L = 4.6$ and $L = 6.8$, lie close to the loss cone boundary (red line in Figure 1) but are still inside the trapped zone. SE energy fluxes presented in Figure 13 correspond to the pitch angles 70° and 90°, which are located deep in the trapped zone (yellow area in Figure 1). Figures 12 and 13 illustrate the considerable differences between energy distribution functions at different pitch angles, especially for energies below 600 eV.

Here it is important to once again recall that in this paper we have introduced the new boundary condition (4) at the edge of the trap zone (as shown in red in Figure 1 as μ_{LC} or $\mu_{0_{LC}}$, depending on pitch angle variables) for

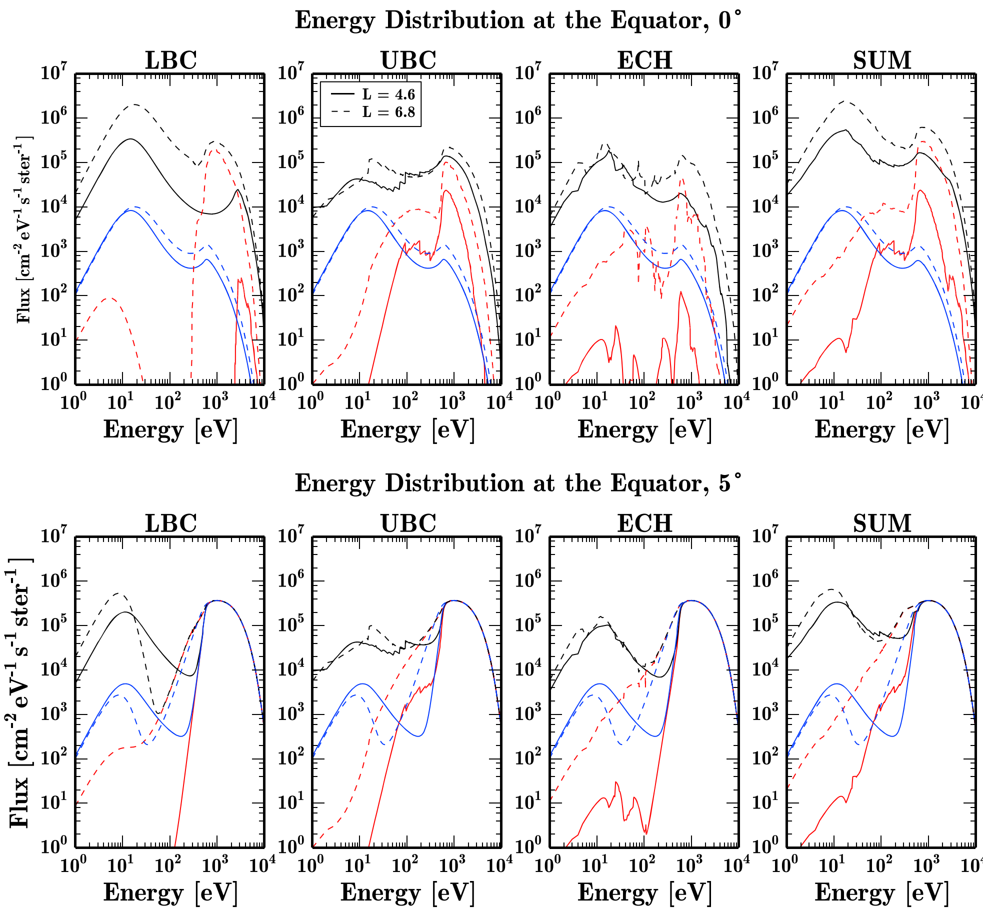

Figure 12. Energy distribution of electron flux from 1 eV to 10 keV at the equator for the pitch angles (top row) 0° and (bottom row) 5°, which is inside the trapped zone but near the loss cone boundary. Cases are presented for L = 4.6 (solid lines) and L = 6.8 (dashed lines) calculated for three types of WPI: (first column) LBC, (second column) UBC, (third column) ECH, and (fourth column) their SUM. Calculations for three scenarios are included: the complete simulation (black), no MI coupling (red), and no wave activity (blue).

the energies $E \geq 600$ eV. In the magnetospheric trapping zone, we kept the energy distribution of SE above 600 eV the same, with the energy spectra (9) and isotropic pitch angle distribution, illustrated in Figures 12 and 13. In the trapped zone for energies below 600 eV and in the loss cone zone for all the energies 1 eV–10 KeV, Figures 12 and 13 indicate considerable differences in SE energy spectra depending on the case studies that are presented in these plots, as well as on the different types of wave activities, LBC, UBC, or ECH.

From Figure 12 it may be noted that the flux at 0° (top row) due to LBC and ECH waves is larger for L = 6.8 (dashed lines) as compared to the case for L = 4.6 (solid lines) in the complete simulation (black). For UBC the fluxes are comparable at the two L shells. This is consistent with $D_{\alpha\alpha}$ calculations presented in Figures 3–7 and discussed earlier. The differences in fluxes for L = 4.6 and 6.8 at 5° (Figure 12, bottom row) are related to the proximity of loss cone angle at L = 4.6 (4.3°) as compared to that for L = 6.8 (2.4°). SE fluxes at 68.8° and 90° shown in Figure 13 are negligibly small for LBC and ECH waves. This can be understood from $D_{\alpha\alpha}$ presented in Figures 3, 5, and 7 for ECH and LBC waves. It may be noted from these figures that, in general, $D_{\alpha\alpha}$ drops to negligibly small values beyond pitch angle 60°. Therefore, SE flux from the loss cone cannot diffuse deep into the trap zone beyond 70°.

However, SE flux due to UBC waves is not so small at 68.8 and 90°. This is consistent with $D_{\alpha\alpha}$ calculations for UBC waves shown in Figures 4 and 6. It is seen that $D_{\alpha\alpha}$ for UBC waves extends almost until pitch angle 90°, allowing SE fluxes from the loss cone to diffuse deeper into the trap zone. Further, it may be noted from Figure 13 for UBC that SE flux is larger for L = 4.6 (solid lines, black) as compared to the case for L = 6.8 (dashed lines, black). This is consistent with $D_{\alpha\alpha}$ calculations shown in Figures 4 and 6.

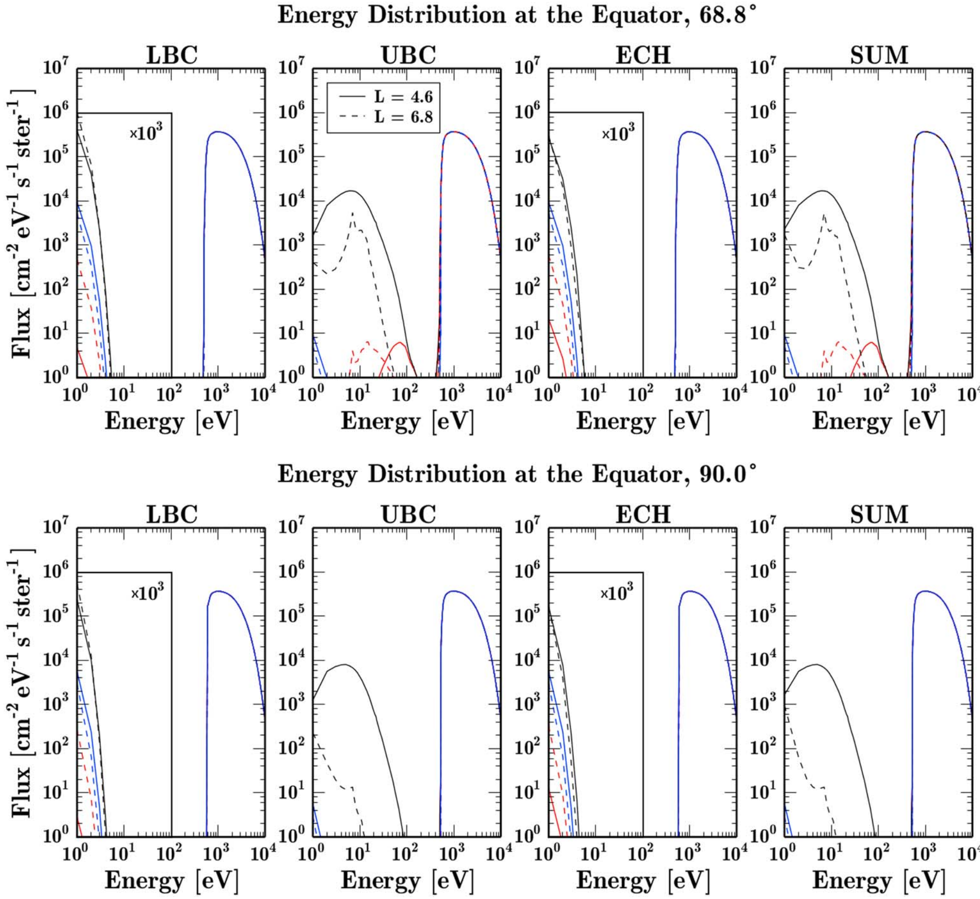

Figure 13. Energy distribution of electron flux from 1 eV to 10 keV at the equator for the pitch angles (top row) 68.8° and (bottom row) 90.0° degrees, which are deep in the trapped zone. Cases are presented for $L = 4.6$ (solid lines) and $L = 6.8$ (dashed lines) calculated for three types of WPI: (first column) LBC, (second column) UBC, (third column) ECH, and (fourth column) their SUM. Calculations for three scenarios are included: the complete simulation (black), no MI coupling (red), and no wave activity (blue). Fluxes below 600 eV are scaled up as indicated on the figure.

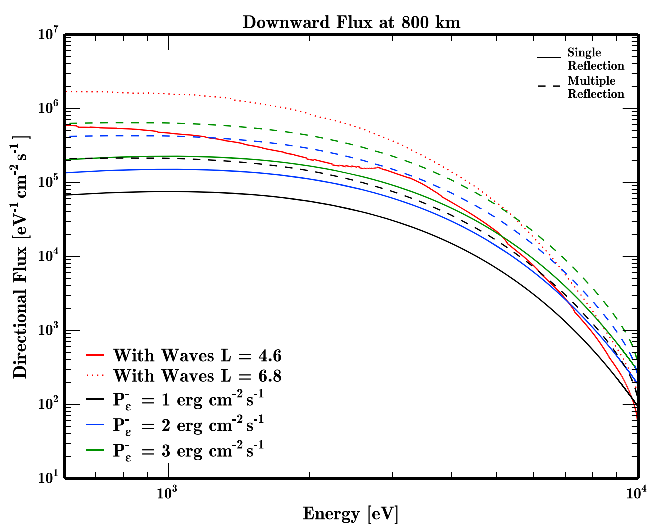

Figure 14. Downward precipitating electron flux from 600 eV to 10 keV at 800 km for three different total precipitating energy fluxes: 1, 2, and 3 erg cm^{-2} s^{-1} (black, blue, and green, respectively) in the case of single (solid lines) and multiple reflection (dashed lines). Red lines also indicate the flux calculated with the new WPI boundary conditions for $L = 4.6$ (solid red line) and $L = 6.8$ (dotted red line). While the cases of single and multiple reflection run nearly parallel to each other, the cases with WPI exhibit a different shape.

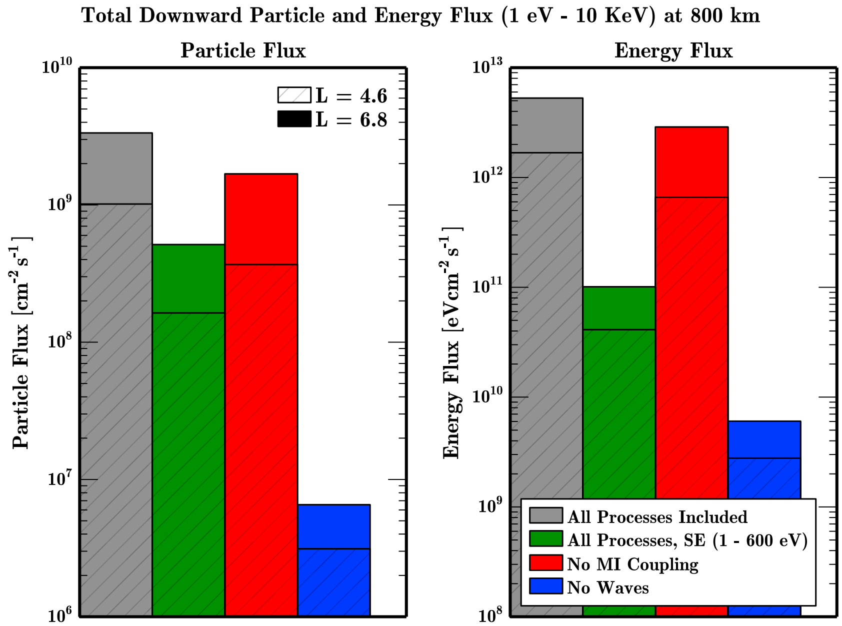

Figure 15. Histogram 1: Downward directional particle (left) and energy (right) flux at 800 km integrated from 1 eV to 10 keV for $L = 4.6$ (dashed bars) and $L = 6.8$ (solid bars) calculated for three scenarios: the complete simulation (gray), no MI coupling (red), and no wave activity (blue). The integrated contribution from SE flux (green) with $E < 600$ eV in the complete simulation is also presented.

Initial expectations for the energy spectra of electrons with energies $E \geq 600$ eV that precipitate into the atmosphere (as presented above in Figures 8 and 9) are that they should be consistent with the corresponding energy spectra of the trapped electron population described by formula (9). This is supported by observations of particles at geosynchronous orbit, observations of the auroral display, and observations of auroral electron precipitation around conjugate field lines, which was observed by DMSP 32, a polar-orbiting satellite, and presented by *Meng et al.* [1979]. The same conclusion could also be made based on the recent theoretical study by *Khazanov et al.* [2015b] where plasma sheet electrons initially injected into atmosphere with a Maxwellian-like energy spectra $\sim AEe^{-E/E_0}$ maintained a very similar spectra in the upper ionosphere

Table 1. Integrated Fluxes (1 eV–10 keV) at 800 km

Waves Included	Direction	Flux Quantity	$L = 6.8$	$L = 4.6$
LBC	Up	Particle	1.52×10^9 (48% of SUM)	1.97×10^8 (20% of SUM)
UBC	Up	Particle	1.10×10^9 (35% of SUM)	6.73×10^8 (70% of SUM)
ECH	Up	Particle	5.50×10^8 (17% of SUM)	9.13×10^7 (10% of SUM)
SUM	Up	Particle	3.17×10^9	1.61×10^8
LBC	Down	Particle	1.63×10^9 (49% of SUM)	2.19×10^8 (22% of SUM)
UBC	Down	Particle	1.15×10^9 (34% of SUM)	7.00×10^8 (69% of SUM)
ECH	Down	Particle	5.69×10^8 (17% of SUM)	9.59×10^7 (9% of SUM)
SUM	Down	Particle	3.35×10^9	1.02×10^8
LBC	Up	Energy	1.80×10^{12} (50% of SUM)	4.34×10^{12} (38% of SUM)
UBC	Up	Energy	1.29×10^{12} (36% of SUM)	6.48×10^{12} (56% of SUM)
ECH	Up	Energy	4.80×10^{11} (13% of SUM)	6.71×10^{11} (6% of SUM)
SUM	Up	Energy	3.57×10^{12}	1.15×10^{12}
LBC	Down	Energy	2.66×10^{12} (50% of SUM)	6.14×10^{11} (37% of SUM)
UBC	Down	Energy	1.90×10^{12} (36% of SUM)	9.66×10^{11} (57% of SUM)
ECH	Down	Energy	7.21×10^{11} (14% of SUM)	1.00×10^{11} (6% of SUM)
SUM	Down	Energy	5.28×10^{12}	1.68×10^{12}

Table 2. Strong Diffusion Rates (s^{-1}) for Electrons With Different Energies at $L = 4.6$ and 6.8

E (keV)	$L = 4.6$	$L = 6.8$
0.5	1.9×10^{-3}	4.0×10^{-4}
1.0	2.8×10^{-3}	5.7×10^{-4}
5.0	6.4×10^{-3}	1.3×10^{-3}
10.0	9.1×10^{-3}	1.8×10^{-3}

after multiple atmospheric reflections from the magnetically conjugated ionospheres. In that study, however, *Khazanov et al.* [2015b] used boundary conditions at the altitude of 800 km that assumed a Maxwellian-like energy spectra isotropic in the downward direction. Here we examine this issue based on the new results presented in this paper to determine whether ECH, LBC, and UBC wave activity, which were described above, produce a Maxwellian-like electron distribution function (9) at upper ionosphere altitudes.

Figure 14 shows fluxes precipitating into the ionosphere that are calculated using a Maxwellian-like diffuse auroral electron spectra (9) with a fixed value of the mean energy parameter E_0 but varying values of the parameter A. The cases shown in Figure 14 are calculated with boundary conditions imposed at the altitude of 800 km, assuming a Maxwellian-like energy spectra $\sim AEe^{-E/E_0}$ as presented by *Khazanov et al.* [2015b]. One case shown is the result of taking into account multiple reflections in the magnetically conjugated ionospheres; additionally shown is the case calculated based on the boundary condition of equation (9), as shown above in Figures 8 and 9. Black, blue, and green solid lines in this figure correspond to the electron flux initially injected into the atmosphere at the altitude of 800 km with precipitating energy fluxes, 1, 2, and 3 erg cm^{-2} s^{-1}, respectively. After accounting for multiple reflections of this initial energy flux injection into both magnetically conjugate regions, as described by *Khazanov et al.* [2015b], the calculated particle downward fluxes are plotted by dashed lines of the same color, labeled Multiple Reflection. Each pair of black, blue, and green solid and dashed lines run nearly parallel, demonstrating the similarity between the energy spectra of the plasma sheet electrons initially injected into the atmosphere and the electrons after their multiple reflections and degradation in both magnetically conjugated ionospheres.

Figure 14 also shows, with a red line, the flux precipitating into the ionosphere that is calculated using the new boundary condition of equation (9) with $A = 10^3$ and $E_0 = 1$ KeV. Based on the assumption of a fully filled loss cone for all energies, as in the case of strong diffusion, this new boundary condition will produce an energy flux into the atmosphere of about 10 erg cm^{-2} s^{-1}. Such an assumption, however, is not realistic, because based on the $D_{\alpha\alpha}$ calculations presented in the section 3, only a small portion of plasma sheet electrons, at some energies, suffers efficient precipitation loss at a rate approaching that of strong diffusion. In Table 2 we present strong diffusion rates at $L = 4.6$ and 6.8 for electron energies 0.5, 1.0, 5.0, and 10.0 keV (e.g., *Tripathi et al.* [2013]). From Figure 4 at $L = 4.6$ it is seen that $D_{\alpha\alpha}$ for UBC just approaches the strong diffusion rate for the energies 0.5 and 1.0 keV. At other energies and other wave modes, $D_{\alpha\alpha}$ is much smaller than the strong diffusion rate. For $L = 6.8$, $D_{\alpha\alpha}$ for ECH waves (Figure 3b) exceeds the strong diffusion rate. For UBC and LBC waves $D_{\alpha\alpha}$ (Figures 6 and 7) approaches or exceeds the strong diffusion rate for 0.5 and 1.0 keV.

In reality, however, based on the pitch angle diffusion coefficients for the ECH, LBC, and UBC waves that have been discussed above, the calculated energy flux in the case presented by the solid red line is 2.6 erg cm^{-2} s^{-1}, for $L = 4.6$, and is considerably bigger, 8.3 erg cm^{-2} s^{-1}, for $L = 6.8$, as shown on Figure 14 by the red dotted line. This represents about 25% and 80%, respectively, of the maximum energy fluxes that could be provided

Table 3. Downward Integrated Fluxes (600 eV – 10 keV) at 800 km

Waves Included	Flux Quantity	$L = 6.8$	$L = 4.6$
LBC	Particle	1.33×10^9 (47% of SUM)	1.89×10^8 (22% of SUM)
UBC	Particle	1.01×10^9 (36% of SUM)	5.94×10^8 (70% of SUM)
ECH	Particle	4.84×10^8 (17% of SUM)	6.84×10^7 (8% of SUM)
SUM	Particle	2.83×10^9	8.52×10^8
LBC	Energy	2.62×10^{12} (50% of SUM)	6.10×10^{11} (37% of SUM)
UBC	Energy	1.87×10^{12} (36% of SUM)	9.35×10^{11} (57% of SUM)
ECH	Energy	6.99×10^{11} (13% of SUM)	9.33×10^{10} (6% of SUM)
SUM	Energy	5.18×10^{12}	1.64×10^{12}

by the electron content of the trap zone in the case of the strong pitch angle diffusion. The shapes of the spectra presented by both types of red lines in Figure 14, unlike the cases of multiple reflection shown in dashed lines, do not run parallel to a solid line of single reflection. This shows that they are only slightly similar to the spectra of electron flux precipitating into the ionosphere after being trapped in the magnetosphere and are described by boundary condition (9) with the constant $E_0 = 1$ KeV. The difference in spectral shape is caused by the complexity of the pitch angle diffusion coefficients for the ECH, LBC, and UBC waves as a function of their energy and pitch angle, which were shown in Figures 3–7.

In addition to providing the spectral shape of electron fluxes with waves, we present, in Table 3, the integrated particle and energy fluxes that correspond exactly to the cases of Figure 14, as well as the partial contribution of each type of wave. Unlike in Table 1 above, the integration in Table 3 is performed over the range 600 eV–10 keV, which corresponds to the energy range of Figure 14. For both the integrated energy and particle fluxes, the majority of flux is again contributed by UBC, ∼60–70%, or LBC, ∼50%, at $L = 4.6$ and $L = 6.8$, respectively. While Figure 14 illustrates the effect on electron spectral shape caused by wave activity, the details of relative wave contribution in Table 3 give insight into their separate mechanisms and simultaneously emphasize the enormous contribution that they make to precipitating flux.

5. Summary and Major Results

The electron diffuse aurora, a precipitation of high-energy magnetospheric electrons due to pitch angle scattering by different kinds of wave-particle interaction in the plasma sheet, is an important source of energy input to the Earth's ionosphere. It provides a significant energy flux into the Earth's ionosphere. It has been found [*Khazanov et al.*, 2014, 2015a, 2015b] that in order to fully understand the formation of this incoming energy flux at the upper ionospheric boundary, ∼700–800 km, it is important to consider the coupled ionosphere-magnetosphere system. The precipitation of magnetospheric electrons in the diffuse aurora is also affiliated with their degradation toward lower energies and the production of secondary electrons. These electrons can additionally be reflected back out of the two magnetically conjugate ionospheres, leading to a series of multiple reflections through the magnetosphere that can greatly enhance the flux precipitating at the upper ionospheric boundary (700–800 km). In this paper, for the first time, we discussed the formation of the electron distribution function in the diffuse auroral region, beginning with the primary injection of plasma sheet electrons via both electron cyclotron harmonic waves and whistler mode chorus waves to the loss cone and including their subsequent multiple atmospheric reflections in the two magnetically conjugated ionospheres.

In our results for electron fluxes, we used numerical diffusion coefficients for three types of waves: ECH (Figure 3), LBC (Figures 5 and 7), and UBC (Figures 4 and 6), the calculation of which is described in section 3. The effect of each individual type of wave activity, as well as their sum, on the precipitating electron energy spectra and total integrated flux at the upper ionospheric boundary was presented in Figure 8 and Histogram 1. The behavior of upward, downward, and omnidirectional fluxes with waves at different ionospheric altitudes for $L = 4.6$ and $L = 6.8$ was examined, both in terms of their energy spectra (Figures 9, 10) and total integrated flux (Figure 11, tabulated in Table 1), and was shown to be consistent with our previous work. The electron spectral energy distribution for different types of wave activity at the equator for various pitch angles near the loss cone (Figure 12) and the trapped zone (Figure 13) was studied and again illustrated the significant effect of wave activity on the electron flux spectral shape. The differences between this spectral shape with wave activity and the initially injected Maxwellian-like primary spectrum was illustrated in Figure 14, and the corresponding effect on total fluxes due to the different types of wave activity was calculated (Table 3). These results have demonstrated that magnetosphere-ionosphere coupling is a key element in the formation of the electron distribution function in the diffuse auroral region and that the inclusion of wave-particle interaction processes in the STET simulation produces a significant effect on precipitating electron spectral shape and magnitude. The inclusion of these processes can be performed in a manner that is consistent with our previous work and with observed data. As mentioned in section 1, the diffuse aurora accounts for about three-quarters of auroral energy precipitating into Earth's ionosphere. Therefore, as we have demonstrated with the analysis in this paper, an approach that includes MI coupling processes and also takes into account the formation of precipitating electron fluxes due to wave-particle interaction is essential to provide a complete picture of ionosphere-magnetosphere energy transfer, a picture which has been left incomplete by both the ionospheric and magnetospheric scientific communities until now.

Appendix A: Collisional Processes

The kinetic equation (1) is gyroaveraged and the collisional terms in $\langle S\rangle$ a gyroaveraging procedure. We adopted notation for all collisional processes following the book by *Khazanov* [2011, chapter 2, equation (2.5.2)]. For their discussion as relevant to this paper, we can present the collisional terms in equation (1) as

Coulomb Collisions With Electrons and Ions

$$\langle S_{ee}\rangle + \langle S_{ei}\rangle = An_e\left\{\frac{\partial}{\partial E}\left(\frac{\Phi}{E}\right) + \frac{1}{2E^2}\frac{\partial}{\partial\mu}\left[(1-\mu^2)\frac{\partial\Phi}{\partial\mu}\right]\right\} \quad \text{(A1)}$$

where n_e is the density of the thermal electrons, $A = 2\pi e^4$, $\ln(L) = 2.6\cdot10^{-12}$ eV^2 cm^2 and $\ln(L)$ is the Coulomb logarithm. The condition of plasma quasi-neutrality ($n_e = n_i$) has been used in arriving at (A1).

Elastic Collisions With Neutral Particles

$$\langle S_{ea}\rangle = n_\alpha\int I_\alpha(E,\chi)\left[\Phi(E,\mu') - \Phi(E,\mu)\right]\mathrm{d}\Omega \quad \text{(A2)}$$

where the scattering $(\mu'\to\mu)$ is described by the scattering angles (χ,η) with $\mu' = \cos\chi\cos\theta + \sin\theta\sin\chi\cos\eta$ and the solid angle $d\Omega = \sin\chi\,\mathrm{d}\chi\mathrm{d}\eta$. The density of neutral particles of species α is n_α and the differential elastic cross section is $I_\alpha(E,\chi)\mathrm{d}\Omega$.

Inelastic Collisions/Excitation

$$\langle S^*_{e\alpha}\rangle = n_\alpha\sum_j\left[\sigma^*_{\alpha j}(E+E^*_{\alpha j})\Phi(E+E^*_{\alpha j}) - \sigma^*_{\alpha j}(E)\Phi(E)\right] \quad \text{(A3)}$$

Inelastic Collisions/Ionization

$$\begin{aligned}\langle S^+_{e\alpha}\rangle = {}& n_\alpha\int_{E+E^+_\alpha}^{2E+E^+_\alpha} I^+_\alpha(E',E'-E-E^+_\alpha)\Phi(E',\mu)\mathrm{d}E' \\ &+ \frac{n_\alpha}{2\pi}\int_{2E+E^+_\alpha}^{\infty} I^+_2(E',E)\int_0^{2\pi}\Phi \\ &\left(E',\sqrt{(1-\mu^2)}\cos\eta\right)\mathrm{d}\eta\mathrm{d}E' - n_\alpha\sigma^+_\alpha(E)\Phi(E,\mu)\end{aligned} \quad \text{(A4)}$$

where E^+_α is ionization energy and $\sigma^*_{\alpha j}$ is the total scattering cross section for exciting neutral particles to a state with threshold energy $E^*_{\alpha j}$. We also have

$$\langle\sigma^+_{e\alpha}\rangle = \int_0^{(E-E^+_\alpha)/2} I^+_\alpha(E,E_2)\mathrm{d}E_2 \quad \text{(A5)}$$

which indicates the total ionization cross section for an electron with energy E. $I^+_\alpha(E,E_2)$ is the relevant differential cross section, and E_2 is secondary electron energy.

Quasi-Linear Interactions with ECH, LBC, and UBC Waves

$$\langle S_{ew}\rangle = \frac{1}{v}\frac{\partial}{\partial\mu}\left[(1-\mu^2)D_{\alpha\alpha}\frac{\partial\Phi}{\partial\mu}\right] \quad \text{(A6)}$$

where $\mu = \cos\alpha$, $\langle S_{ew}\rangle$ is the part of $\langle S\rangle$ in (1) that denotes the interaction of SE with ECH, LBC, and UBC waves, and the local pitch angle diffusion coefficient $D_{\alpha\alpha}$ is as discussed in section 3.

The transformation of local pitch angle diffusion coefficient $D_{\alpha\alpha}$ into $s-\mu_0$ space in order to solve equation (1) is performed with the equatorial variable $\mu_0 = \cos\alpha_0$ and takes the form

$$D_{\alpha\alpha} = \frac{\cos^2\alpha_0}{\gamma - \sin^2\alpha_0}D_{\alpha_0\alpha_0} \quad \text{(A7)}$$

where the equatorial pitch angle α_0 is connected by the first adiabatic invariant and the relation $\gamma = B_0/B(S)$ to the local pitch angle α.

Acknowledgments
Funding support for this study was provided by NASA Van Allen Probes (formerly known as the Radiation Belt Storm Probes (RBSP)) Project, the NASA LWS Program, and by Indian Institute of Technology (Banaras Hindu University), India. The data for this paper are available from George V. Khazanov at george.v.khazanov@nasa.gov.

References

Anderson, R. R., and K. Maeda (1977), VLF emissions associated with enhanced magnetospheric electrons, *J. Geophys. Res.*, *82*, 135–146, doi:10.1029/JA082i001p00135.

Ashour-Abdalla, M., and C. F. Kennel (1978), Nonconvective and convective electron cyclotron harmonic instabilities, *J. Geophys. Res.*, *83*, 1531–1543, doi:10.1029/JA083iA04p01531.

Bame, S. J., J. R. Asbridge, H. E. Felthauser, E. W. Hones, and I. B. Strong (1967), Characteristics of the plasma sheet in the Earth's magnetotail, *J. Geophys. Res.*, *72*, 113–129, doi:10.1029/JZ072i001p00113.

Banks, P. M., C. R. Chappell, and A. F. Nagy (1974), A new model for the interaction of auroral electrons with the atmosphere: Spectral degradation, backscatter, optical emission, and ionization, *J. Geophys. Res.*, *79*, 1459–1470, doi:10.1029/JA079i010p01459.

Belmont, G., D. Fontaine, and P. Canu (1983), Are equatorial electron cyclotron waves responsible for diffuse auroral electron precipitation?, *J. Geophys. Res.*, *88*, 9163–9170, doi:10.1029/JA088iA11p09163.

Belmont, G., D. Fontaine, and P. Canu (1984), Reply [to "Comment on 'Are equatorial electron cyclotron waves responsible for diffuse auroral electron precipitation?' by G. Belmont, D. Fontaine, and P. Canu"], *J. Geophys. Res.*, *89*, 7591–7591, doi:10.1029/JA089iA09p07591.

Bilitza, D. (1990), Progress report on IRI status, *Adv. Space Res.*, *10*, 3–5, doi:10.1016/0273-1177(90)90298-E.

Buonsanto, M. J. (1989), Comparison of incoherent scatter observations of electron density, and electron and ion temperature at Millstone Hill with the international reference ionosphere, *J. Atmos. Terr. Phys.*, *51*, 441–468.

Burtis, W. J., and R. A. Helliwell (1969), Banded chorus—A new type of VLF radiation observed in the magnetosphere by OGO 1 and OGO 3, *J. Geophys. Res.*, *74*, 3002–3010, doi:10.1029/JA074i011p03002.

Decker, D. T., D. N. Anderson, and A. J. Preble (1997), Improving IRI-90 low-latitude electron density specification, *Rad. Sci.*, *32*, 2003–2019, doi:10.1029/97RS01029.

Fontaine, D., and M. Blanc (1983), A theoretical approach to the morphology and the dynamics of diffuse auroral zones, *J. Geophys. Res.*, *88*, 7171–7184, doi:10.1029/JA088iA09p07171.

Glauert, S., and R. Horne (2005), Calculation of pitch angle and energy diffusion coefficients with the PADIE code, *J. Geophys. Res.*, *110*, A04206, doi:10.1029/2004JA010851.

Hardy, D., M. Gussenhoven, and E. Holeman (1985), A statistical model of auroral electron precipitation, *J. Geophys. Res.*, *90*, 4229–4248.

Hardy, D. A., M. S. Gussenhoven, and D. Brautigam (1989), A statistical model of auroral ion precipitation, *J. Geophys. Res.*, *94*, 370–392, doi:10.1029/JA094iA01p00370.

Hedin, A. (1991), Extension of the MSIS thermosphere model into the middle and lower atmosphere, *J. Geophys. Res.*, *96*, 1159–1172.

Horne, R. B. (1989), Path-integrated growth of electrostatic waves—The generation of terrestrial myriametric radiation, *J. Geophys. Res.*, *94*, 8895–8909, doi:10.1029/JA094iA07p08895.

Horne, R. B., and R. M. Thorne (2000), Electron pitch angle diffusion by electrostatic electron cyclotron harmonic waves: The origin of pancake distributions, *J. Geophys. Res.*, *105*, 5391–5402, doi:10.1029/1999JA900447.

Horne, R. B., R. M. Thorne, N. P. Meredith, and R. R. Anderson (2003), Diffuse auroral electron scattering by electron cyclotron harmonic and whistler mode waves during an isolated substorm, *J. Geophys. Res.*, *108*(A7), 1290, doi:10.1029/2002JA009736.

Johnstone, A. D., D. M. Walton, R. Liu, and D. A. Hardy (1993), Pitch angle diffusion of low-energy electrons by whistler mode waves, *J. Geophys. Res.*, *98*, 5959–5967, doi:10.1029/92JA02376.

Kennel, C. F., and H. E. Petschek (1966), Limit on stably trapped particle fluxes, *J. Geophys. Res.*, *71*, 1–28.

Kennel, C. F., F. L. Scarf, R. W. Fredricks, J. H. McGehee, and F. V. Coroniti (1970), VLF electric field observations in the magnetosphere, *J. Geophys. Res.*, *75*, 6136–6152, doi:10.1029/JA075i031p06136.

Khazanov, G. (1979), The kinetics of the electron plasma component of the upper atmosphere. Nakua, Moscow, english Translation: Washington, D. C., National Translation Center 80-50707, 1980.

Khazanov, G. (2011), *Kinetic Theory of the Inner Magnetospheric Plasma, Astrophys. Space Sci. Lib.*, Springer, New York.

Khazanov, G., and M. W. Liemohn (1995), Nonsteady state ionosphere-plasmasphere coupling of superthermal electrons, *J. Geophys. Res.*, *100*, 9669–9681.

Khazanov, G., M. W. Liemohn, T. I. Gombosi, and A. F. Nagy (1993), Non-steady-state transport of superthermal electrons in the plasmasphere, *Geophys. Res. Lett.*, *20*, 2821–2824.

Khazanov, G., T. E. Moore, M. W. Liemohn, V. K. Jordanova, and M.-C. Fok (1996), Global collisional model of high-energy photoelectrons, *Geophys. Res. Lett.*, *23*, 331–334.

Khazanov, G. V., T. I. Gombosi, and A. F. Nagy (1992), Heating and cooling of the plasmasphere, paper presented at AGU Spring Meeting, Montreal, Canada, 12–16 May.

Khazanov, G. V., T. Neubert, and G. D. Gefan (1994), Unified theory of ionosphere-plasmasphere transport of suprathermal electrons, *IEEE Trans. Plasma Sci.*, *22*, 187–198, doi:10.1109/27.279022.

Khazanov, G. V., M. W. Liemohn, E. N. Krivorutsky, J. U. Kozyra, and B. E. Gilchrist (1999), Interhemispheric transport of relativistic electron beams, *Geophys. Res. Lett.*, *26*, 581–584, doi:10.1029/1999GL900045.

Khazanov, G. V., I. K. Khabibrakhmanov, and A. Glocer (2012), Kinetic description of ionospheric outflows based on the exact form of Fokker-Planck collision operator: Electrons, *J. Geophys. Res.*, *117*, A11203, doi:10.1029/2012JA018082.

Khazanov, G. V., A. Glocer, M. W. Liemohn, and E. W. Himwich (2013), Superthermal electron energy interchange in the ionosphere-plasmasphere system, *J. Geophys. Res. Space Physics*, *118*, 925–934, doi:10.1002/jgra.50127.

Khazanov, G. V., A. Glocer, and E. W. Himwich (2014), Magnetosphere-ionosphere energy interchange in the electron diffuse aurora, *J. Geophys. Res. Space Physics*, *119*, 171–184, doi:10.1002/2013JA019325.

Khazanov, G. V., A. K. Tripathi, R. P. Singhal, E. W. Himwich, A. Glocer, and D. G. Sibeck (2015a), Superthermal electron magnetosphere-ionosphere coupling in the diffuse aurora in the presence of ECH waves, *J. Geophys. Res. Space Physics*, *120*, 445–459, doi:10.1002/2014JA020641.

Khazanov, G. V., E. W. Himwich, A. Glocer, and D. G. Sibeck (2015b), The role of multiple atmospheric reflections in the formation of the electron distrubution function in the diffuse aurora region, *AGU Monograph*.

Li, W., R. M. Thorne, V. Angelopoulos, J. Bortnik, C. M. Cully, B. Ni, O. LeContel, A. Roux, U. Auster, and W. Magnes (2009), Global distribution of whistler-mode chorus waves observed on the THEMIS spacecraft, *Geophys. Res. Lett.*, *36*, L09104, doi:10.1029/2009GL037595.

Li, W., B. Ni, R. M. Thorne, J. Bortnik, J. C. Green, C. A. Kletzing, W. S. Kurth, and G. B. Hospodarsky (2013), Constructing the global distribution of chorus wave intensity using measurements of electrons by the POES satellites and waves by the Van Allen Probes, *Geophys. Res. Lett.*, *40*, 4526–4532, doi:10.1002/grl.50920.

Link, R. (1992), Feautrier solution of the electron transport equation, *J. Geophys. Res.*, *97*, 159–169, doi:10.1029/91JA02214.

Lui, A. T. Y., S.-I. Akasofu, D. Venkatesan, C. D. Anger, W. J. Heikkila, J. D. Winningham, and J. R. Burrows (1977), Simultaneous observations of particle precipitations and auroral emissions by the Isis 2 satellite in the 19–24 MLT sector, *J. Geophys. Res.*, *82*, 2210–2226, doi:10.1029/JA082i016p02210.

Lummerzheim, D., and J. Lilensten (1994), Electron transport and energy degradation in the ionosphere: Evaluation of the numerical solution, comparison with laboratory experiments and auroral observations, *Ann. Geophys.*, *12*, 1039–1051, doi:10.1007/s00585-994-1039-7.

Lyons, L. R. (1974a), Electron diffusion driven by magnetospheric electrostatic waves, *J. Geophys. Res.*, *79*, 575–580, doi:10.1029/JA079i004p00575.

Lyons, L. R. (1974b), Pitch angle and energy diffusion coefficients from resonant interactions with ion-cyclotron and whistler waves, *J. Plasma Phys.*, *12*, 417–432, doi:10.1017/S002237780002537X.

Lyons, M. G. (1984), Comment on "A comparison of control techniques for large flexible systems", *J. Guid. Control Dyn.*, *7*, 637–637, doi:10.2514/3.56378.

Meng, C.-I., B. Mauk, and C. E. McIlwain (1979), Electron precipitation of evening diffuse aurora and its conjugate electron fluxes near the magnetospheric equator, *J. Geophys. Res.*, *84*, 2545–2558, doi:10.1029/JA084iA06p02545.

Meredith, N. P., A. D. Johnstone, S. Szita, R. B. Horne, and R. R. Anderson (1999), "Pancake" electron distributions in the outer radiation belts, *J. Geophys. Res.*, *104*, 12,431–12,444, doi:10.1029/1998JA900083.

Meredith, N. P., R. B. Horne, A. D. Johnstone, and R. R. Anderson (2000), The temporal evolution of electron distributions and associated wave activity following substorm injections in the inner magnetosphere, *J. Geophys. Res.*, *105*, 12,907–12,918, doi:10.1029/2000JA900010.

Meredith, N. P., R. B. Horne, R. M. Thorne, and R. R. Anderson (2009), Survey of upper band chorus and ECH waves: Implications for the diffuse aurora, *J. Geophys. Res.*, *114*, A07218, doi:10.1029/2009JA014230.

Meredith, N. P., R. B. Horne, A. Sicard-Piet, D. Boscher, K. H. Yearby, W. Li, and R. M. Thorne (2012), Global model of lower band and upper band chorus from multiple satellite observations, *J. Geophys. Res.*, *117*, A10225, doi:10.1029/2012JA017978.

Min, Q.-L., D. Lummerzheim, M. H. Rees, and K. Stamnes (1993), Effects of a parallel electric field and the geomagnetic field in the topside ionosphere on auroral and photoelectron energy distributions, *J. Geophys. Res.*, *98*, 19,223–19,234, doi:10.1029/93JA01742.

Moore, T. E., and R. L. Arnoldy (1982), Plasma pitch angle distributions near the substorm injection front, *J. Geophys. Res.*, *87*, 265–270, doi:10.1029/JA087iA01p00265.

Newell, P. T., T. Sotirelis, and S. Wing (2009), Diffuse, monoenergetic, and broadband aurora: The global precipitation budget, *J. Geophys. Res.*, *114*, A09207, doi:10.1029/2009JA014326.

Ni, B., R. M. Thorne, Y. Y. Shprits, and J. Bortnik (2008), Resonant scattering of plasma sheet electrons by whistler-mode chorus: Contribution to diffuse auroral precipitation, *Geophys. Res. Lett.*, *35*, L11106, doi:10.1029/2008GL034032.

Ni, B., R. M. Thorne, R. B. Horne, N. P. Meredith, Y. Y. Shprits, L. Chen, and W. Li (2011a), Resonant scattering of plasma sheet electrons leading to diffuse auroral precipitation: 1. Evaluation for electrostatic electron cyclotron harmonic waves, *J. Geophys. Res.*, *116*, A04218, doi:10.1029/2010JA016232.

Ni, B., R. M. Thorne, N. P. Meredith, R. B. Horne, and Y. Y. Shprits (2011b), Resonant scattering of plasma sheet electrons leading to diffuse auroral precipitation: 2. Evaluation for whistler mode chorus waves, *J. Geophys. Res.*, *116*, A04219, doi:10.1029/2010JA016233.

Ni, B., J. Liang, R. M. Thorne, V. Angelopoulos, R. B. Horne, M. Kubyshkina, E. Spanswick, E. F. Donovan, and D. Lummerzheim (2012), Efficient diffuse auroral electron scattering by electrostatic electron cyclotron harmonic waves in the outer magnetosphere: A detailed case study, *J. Geophys. Res.*, *117*, A01218, doi:10.1029/2011JA017095.

Omura, Y., M. Hikishima, Y. Katoh, D. Summers, and S. Yagitani (2009), Nonlinear mechanisms of lower-band and upper-band VLF chorus emissions in the magnetosphere, *J. Geophys. Res.*, *114*, A07217, doi:10.1029/2009JA014206.

Peticolas, L., and D. Lummerzheim (2000), Time-dependent transport of field-aligned bursts of electrons in flickering aurora, *J. Geophys. Res.*, *105*, 12,895–12,906, doi:10.1029/1999JA000398.

Rees, D. (1989), *Physics and Chemistry of the Upper Atmosphere*, Cambridge Univ. Press, New York.

Roeder, J. L., and H. C. Koons (1989), A survey of electron cyclotron waves in the magnetosphere and the diffuse auroral electron precipitation, *J. Geophys. Res.*, *94*, 2529–2541, doi:10.1029/JA094iA03p02529.

Ronnmark, K., H. Borg, P. J. Christiansen, M. P. Gough, and D. Jones (1978), Banded electron cyclotron harmonic instability—A first comparison of theory and experiment, *Space Sci. Rev.*, *22*, 401–417, doi:10.1007/BF00210876.

Runov, A., V. Angelopoulos, C. Gabrielse, J. Liu, D. L. Turner, and X. Z. Zhou (2015), Average thermodynamic and spectral properties of plasma in and around dipolarizing flux bundles, *J. Geophys. Res. Space Physics*, *120*, 4369–4383, doi:10.1002/2015JA021166.

Sandford, P. B. (1968), Variations of auroral emissions with time, magnetic activity and the solar cycle, *J. Atmos. Terr. Phys.*, *30*, 1921–1942, doi:10.1016/0021-9169(68)90001-9.

Shprits, Y. Y., and B. Ni (2009), Dependence of the quasi-linear scattering rates on the wave normal distribution of chorus waves, *J. Geophys. Res.*, *114*, A11205, doi:10.1029/2009JA014223.

Singhal, R. P., and A. K. Tripathi (2006), Study of whistler mode instability in Saturn's magnetosphere, *Ann. Geophys.*, *24*, 1705–1712, doi:10.5194/angeo-24-1705-2006.

Solomon, S., P. Hays, and V. Abreu (1988), The auroral 6300Å emission: Observations and modeling, *J. Geophys. Res.*, *93*, 9867–9882.

Solomon, S. C. (1993), Auroral electron transport using the Monte Carlo method, *Geophys. Res. Lett.*, *20*, 185–188, doi:10.1029/93GL00081.

Stamnes, K. (1981), On the two-stream approach to electron transport and thermalization, *J. Geophys. Res.*, *86*, 2405–2410, doi:10.1029/JA086iA04p02405.

Stix, T. H. (1962), *The Theory of Plasma Waves*, McGraw-Hill, New York.

Strickland, D. J., D. L. Book, T. P. Coffey, and J. A. Fedder (1976), Transport equation techniques for the deposition of auroral electrons, *J. Geophys. Res.*, *81*, 2755–2764, doi:10.1029/JA081i016p02755.

Su, Z., H. Zheng, and S. Wang (2009), Evolution of electron pitch angle distribution due to interactions with whistler mode chorus following substorm injections, *J. Geophys. Res.*, *114*, A08202, doi:10.1029/2009JA014269.

Su, Z., H. Zheng, and S. Wang (2010), A parametric study on the diffuse auroral precipitation by resonant interaction with whistler mode chorus, *J. Geophys. Res.*, *115*, A05219, doi:10.1029/2009JA014759.

Tao, X., R. M. Thorne, W. Li, B. Ni, N. P. Meredith, and R. B. Horne (2011), Evolution of electron pitch angle distributions following injection from the plasma sheet, *J. Geophys. Res.*, *116*, A04229, doi:10.1029/2010JA016245.

Thorne, R. M., B. Ni, X. Tao, R. B. Horne, and N. P. Meredith (2010), Scattering by chorus waves as the dominant cause of diffuse auroral precipitation, *Nature*, *467*, 943–946.

Tripathi, A. K., and R. P. Singhal (2005), Electrostatic electron cyclotron harmonic instability due to energetic electrons in Jupiter's magnetosphere, *J. Geophys. Res.*, *110*, A12205, doi:10.1029/2005JA011113.

Tripathi, A. K., and R. P. Singhal (2009), Diffusion coefficients from resonant interactions with electrostatic electron cyclotron harmonic waves, *Phys. Plasmas*, *16*(11), 112107, doi:10.1063/1.3264735.

Tripathi, A. K., R. P. Singhal, K. P. Singh, and O. N. Singh (2013), Diffuse auroral precipitation by resonant interaction with electron cyclotron harmonic and whistler mode waves, *J. Atmos. Sol. Terr. Phys.*, *97*, 125–134, doi:10.1016/j.jastp.2013.01.013.
Tripathi, A. K., R. P. Singhal, K. P. Singh, and O. N. Singh (2014a), Electrostatic electron cyclotron harmonic instability near Ganymede, *Astrophys. Space Sci.*, *352*, 421–427, doi:10.1007/s10509-014-1957-0.
Tripathi, A. K., R. P. Singhal, K. P. Singh, and O. N. Singh (2014b), Whistler mode instability and pitch-angle diffusion near Ganymede, *Planet. Space Sci.*, *92*, 150–156, doi:10.1016/j.pss.2014.01.005.
Wrenn, G. L., J. F. E. Johnson, and J. J. Sojka (1979), Stable "pancake" distributions of low energy electrons in the plasma trough, *Nature*, *279*, 512–514, doi:10.1038/279512a0.
Zhang, X., and V. Angelopoulos (2014), On the relationship of electrostatic cyclotron harmonic emissions with electron injections and dipolarization fronts, *J. Geophys. Res. Space Physics*, *119*, 2536–2549, doi:10.1002/2013JA019540.
Zhang, X., V. Angelopoulos, B. Ni, R. M. Thorne, and R. B. Horne (2013), Quasi-steady, marginally unstable electron cyclotron harmonic wave amplitudes, *J. Geophys. Res. Space Physics*, *118*, 3165–3172, doi:10.1002/jgra.50319.
Zhang, X.-J., V. Angelopoulos, B. Ni, and R. M. Thorne (2015), Predominance of ECH wave contribution to diffuse aurora in Earth's outer magnetosphere, *J. Geophys. Res. Space Physics*, *120*, 295–309, doi:10.1002/2014JA020455.